Article

Zn^{2+} and Cu^{2+} Interaction with the Recognition Interface of ACE2 for SARS-CoV-2 Spike Protein

Alessio Pelucelli [1*], Massimiliano Peana [1*], Bartosz Orzeł [2], Elzbieta Gumienna-Kontecka [2], Serenella Medici and Maria Antonietta Zoroddu [1]

[1] Department of Chemical, Physical, Mathematical and Natural Sciences, University of Sassari, 07100 Sassari, Italy; A.P. alessiopelucelli@gmail.com; M.P. peana@uniss.it; S.M. sere@uniss.it; M.A.Z. zoroddu@uniss.it

[2] Faculty of Chemistry, University of Wroclaw, 50-383 Wroclaw, Poland; B.O. bartosz.orzel@chem.uni.wroc.pl; E.G.K. elzbieta.gumienna-kontecka@chem.uni.wroc.pl

* Correspondence: peana@uniss.it) (M.P.), alessiopelucelli@gmail.com (A.P.)

Abstract: The spike protein (S) of SARS-CoV-2 has been shown to bind to the human angiotensin-converting enzyme 2 (ACE2) receptor with much higher affinity compared to other coronaviruses. The binding interface between the ACE2 receptor plays a critical role in the entry mechanism of SARS-CoV-2 virus. There are specific amino acids involved in the interaction between S protein and ACE2 receptor. This specificity is critical for the virus to establish a systemic infection and cause COVID-19 disease. In the ACE2 receptor, the largest number of amino acids that play a crucial role in the mechanism of interaction and recognition with the S protein are located in the C-terminal part which represents the main binding region between ACE2 and S. This fragment is abundant in coordination residues such as aspartates, glutamates and histidine that could be targeted by metal ions. Zn^{2+} ion binds to the ACE2 receptor in its catalytic site and modulates its activity, but it could also contribute to the structural stability of the entire protein. The ability of the human ACE2 receptor to coordinate metal ions, such Zn^{2+}, in the same region where it binds to the S protein could have a crucial impact in the mechanism of recognition and interaction of ACE2-S with consequences on their binding affinity that deserve to be investigated. To test this possibility, this study aims to characterize the coordination ability of Zn^{2+}, and also Cu^{2+} for comparison, with selected peptide models of the ACE2 binding interface using spectroscopic and potentiometric techniques.

Keywords: ACE2; peptides; zinc complexes; copper complexes; metal interaction; potentiometry; spectroscopy; NMR

1. Introduction

The human angiotensin-converting enzyme 2 (ACE2) receptor plays a critical role in regulating blood pressure, but it has gained notoriety as the key entry point for the SARS-CoV-2 virus that causes COVID-19. This protein acts as a receptor for the virus, allowing it to enter and infect human cells [1]. ACE2 receptor is expressed in various tissues including the lungs, heart, and kidneys, making it a crucial target for the virus to establish a systemic infection [2].

ACE2 receptor is a type I transmembrane protein belonging to the family of carboxypeptidase enzymes. It has several functions, including regulating blood pressure by converting angiotensin II into angiotensin-(1-7), which has vasodilatory effects. Additionally, it has a protective effect on the heart and kidneys, making it a potential therapeutic target to treat cardiovascular and renal diseases [3].

SARS-CoV-2 spike protein (S) interacts with ACE2 receptor acting as a key and allowing the virus to enter and infect human cells. The spike is a trimeric structure composed of three identical subunits and it contains two domains, the N-terminal S1 domain, and the C-terminal S2 domain. The S1 domain mediates S protein binding to ACE2 receptor, while the S2 domain is responsible for the

Preprints (www.preprints.org) | NOT PEER-REVIEWED | Posted: 4 May 2023 doi:10.20944/preprints202305.0226.v1

fusion between virus and host cell membranes [4]. The interaction between the spike protein and ACE2 receptor is now well documented. Spike protein binds to ACE2 receptor with high affinity, allowing the virus to enter host cells and replicate therein [1,2,5]. Such interaction results in the loss of ACE2 function and the increase of angiotensin II levels, leading to a state of hypertension and increased oxidative stress, which contributes to the severity of COVID-19. Studies have shown that the number of ACE2 receptors in certain tissues can affect the severity of COVID-19 [6]. For example, individuals with higher levels of ACE2 expression in the lungs are more susceptible to severe respiratory distress, while higher expression in the heart can lead to a higher risk of cardiovascular complications. Moreover, certain genetic variations in the ACE2 gene have been associated with an increased risk of severe disease in COVID-19 patients [6].

The ACE2-S bond is a critical aspect of the ability of SARS-CoV-2 virus to infect human cells and cause COVID-19 [7], since their interaction is specific and highly affinity driven [8], much higher than other coronaviruses [9]. This specificity is critical for the virus to establish a systemic infection and cause disease.

The structure of ACE2 receptor is also critical for the interaction with S protein. ACE2 receptor exists in multiple conformations, and the preferred conformation for S binding has been identified as a closed and compact form. This conformation allows for optimal interaction between the amino acids of ACE2 receptor and the S1 domain and provides the highest binding affinity between the two proteins. The exact details of the preferred conformation of the ACE2 receptor, such as the specific arrangement of amino acids and interactions, are still the subject of ongoing research. Mutations in the S protein can affect its ability to bind ACE2 receptor and reduce the infectivity of the virus [10], but also the other way around.

Understanding the details of this interaction is crucial for the development of therapies to prevent and treat COVID-19. In fact, although the massive vaccination campaigns decreased the mortality associated with COVID-19 all over the world and the virus is now circulating freely with symptoms similar to a normal cold or flu, there is still a part of the population suffering from severe complications after infection, and the emergence of new mutation cannot be excluded [11]. Thus, further research is needed to fully understand the mechanisms behind the spike-ACE2 receptor interaction and how it contributes to the severity of the disease.

The specific amino acids involved in the interaction between the S protein and ACE2 receptor have been identified. The ACE2-S binding is primarily driven by the S1 domain of the S protein, and several amino acids in this interface seem to play a critical role in the recognition and binding process [12].

The analysis of the structural basis of receptor recognition by SARS-CoV-2 evidenced that residues N487, Q493, Y505, Y499, T500 and G446 of RBD (Receptor-Binding Domain) in the S protein are the recurrent amino acids which can make a direct contribution to the affinity of the ACE2-S interaction (Figure 1) [12,13]. These residues are involved in hydrogen bonding with the ACE2 receptor, and mutations in those positions have appear to reduce the binding affinity between the two proteins [14].

Likewise, also some specific residues in the ACE2 receptor play a crucial role in the interaction: Q24, D30, H34, E35, E37, D38, Y41, and Q42 (Figure 1) [15,16]. These amino acids are involved in the formation of a network of hydrogen bonds with the specific residues of S protein, already mentioned, and mutations at these positions seem to weaken the binding between the two proteins, as well. These residues are located in the C-terminal part of ACE2 which represents the main interface region between ACE2 and S: $S_{19}T_{20}I_{21}E_{22}E_{23}Q_{24}A_{25}K_{26}T_{27}F_{28}L_{29}D_{30}K_{31}F_{32}N_{33}H_{34}E_{35}A_{36}E_{37}D_{38}L_{39}F_{40}Y_{41}Q_{42}$.

Preprints (www.preprints.org) | NOT PEER-REVIEWED | Posted: 4 May 2023 doi:10.20944/preprints202305.0226.v1

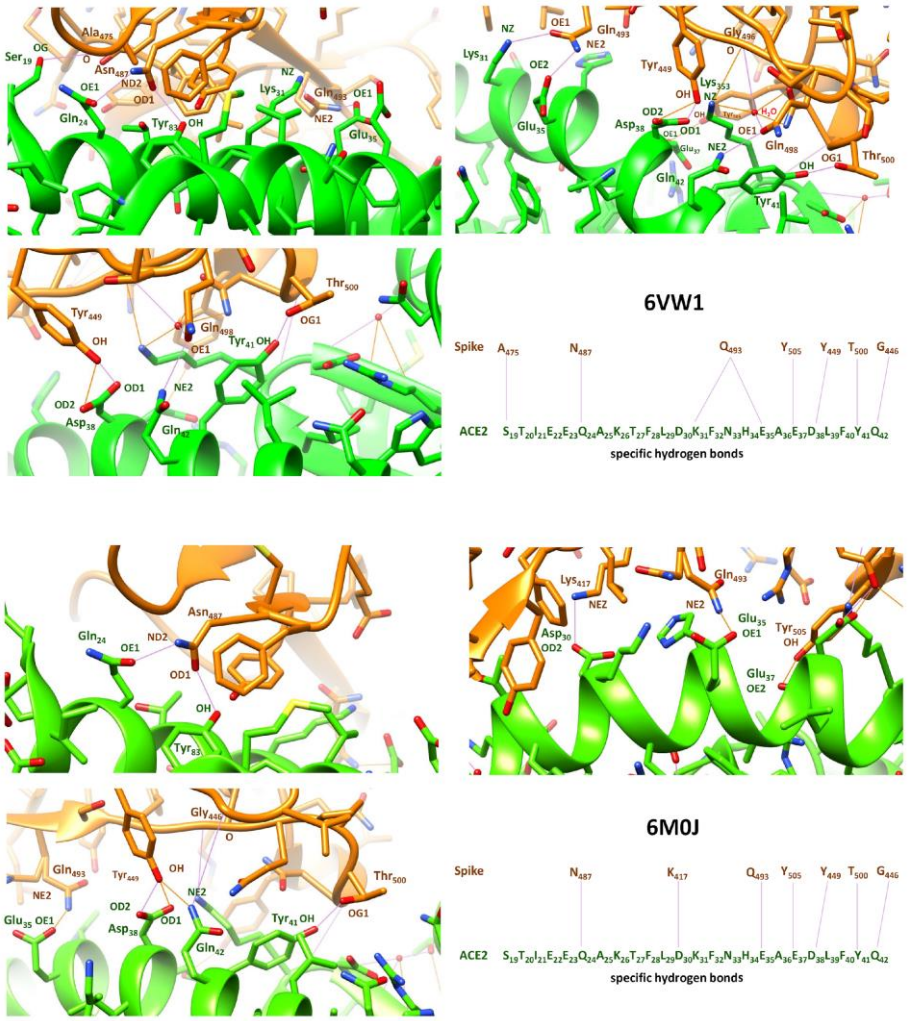

Figure 1. Specific hydrogen bonds between the RBD of SARS-CoV-2 and the binding interface of ACE2, extracted from the X-ray structures with PDB code 6VW1 [13] and 6M0J [12].

A growing body of evidence supports that zinc deficiency is one of the major determinants of COVID-19 risk and severity [17]. Zn^{2+} binds to specific residues ($H_{374}E_{402}XXH_{378}$) in ACE2 modulating its activity [18], and is also able to modify the conformation of the receptor [19]. What is particularly interesting in the interface region of ACE2 is the abundance of amino acids such as aspartates, glutamates, and histidine with peculiar and selective coordinating ability. With regards to the interaction between ACE2 and S protein of SARS-CoV-2, it is thought that the coordination of metal ions could alter the conformation of ACE2 and thus modify its affinity for the S protein. In particular, the ability of human ACE2 receptor to coordinate metal ions in the same region where it binds to the S protein of SARS-CoV-2 could have a crucial impact in the mechanism of recognition and interaction of the two proteins with repercussions on their binding affinity that deserve to be investigated. We preliminarily tested the ability of the interface region of ACE2 to bind Zn^{2+} ions using MIB2, a metal ion binding site prediction and modeling server, which performs metal ion docking and predicts metal binding residues from deposited structures at X-ray [20]. The results were promising, as we could observe that a recurrent interaction pattern was present even considering different ACE2 and S-ACE2 structures [21-25]. In particular, the region with a high Zn^{2+} binding probability involved amino acids comprising the 30-37 sequence, which consists of a rich set of coordinating residues, $D_{30}KFNHEAE_{37}$ (Figure 2).

Preprints (www.preprints.org) | NOT PEER-REVIEWED | Posted: 4 May 2023 doi:10.20944/preprints202305.0226.v1

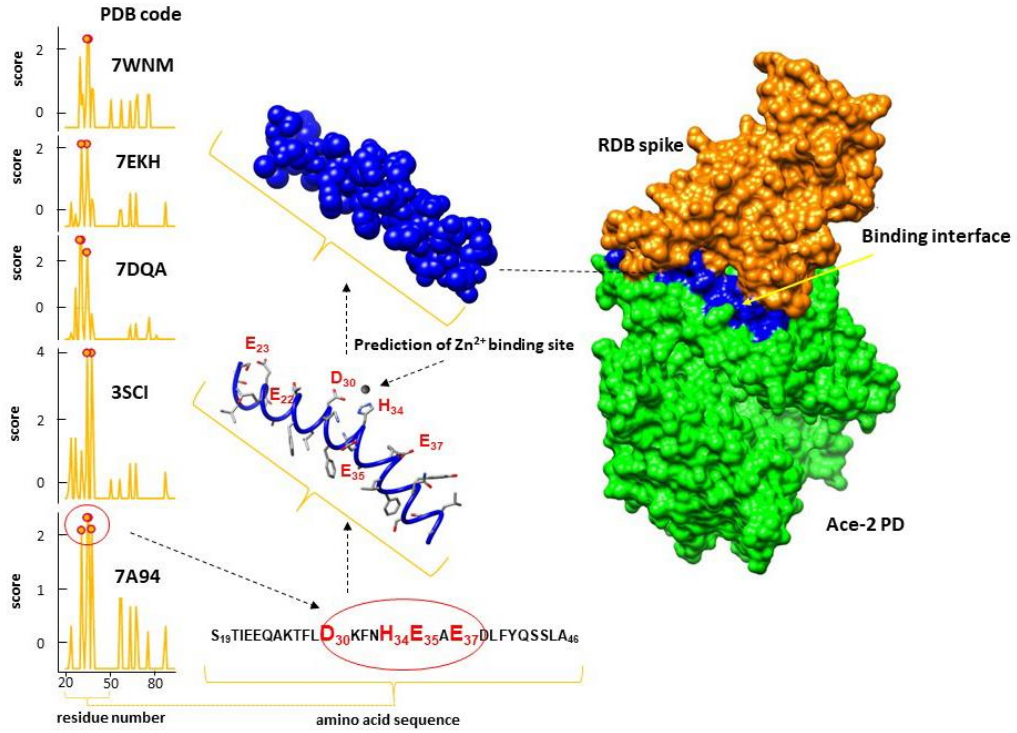

Figure 2. MIB2 prediction of Zn ion-binding sites (in the range 19 to 100) from a selection of ACE2 X-ray structures (PDB 7A94, 3SCI, 7DQA, 7EKH and 7WNM) [21-25]. MIB2 combines both structural and sequence information to identify the local structure of protein-metal interaction sites. The plot on the left showed the residues scoring above the threshold that are predicted to be metal-binding residues. The residues recurrent in all predictions are located in the binding interface between ACE2 and the S protein, localized in the fragment 30-37 aa.

In order to test this hypothesis, the present study aims to characterize the coordination ability of Zn^{2+} ions with selected peptide fragments of the binding interface of ACE2. In particular, we selected three sequence models: P29-38 (Ac-L_{29}DKFNHEAED$_{38}$-NH_2), P23-42 (Ac-E_{23}QAKTFL$_{29}$DKFNHEAED$_{38}$LFYQ$_{42}$-NH_2), and P19-42 (Ac-S_{19}TIEEQAKTFL$_{29}$DKFNHEAED$_{38}$LFYQ$_{42}$-NH_2). Peptide P29-38 contains, according to MIB2 prediction, the interacting sequence able to bind Zn^{2+}. The other two peptides, P23-42 and P19-42, are larger models of the recognition region of the two proteins, and both include the sequence of P29-38. The longest peptide, P19-42, represents the whole binding interface of ACE2. We studied, through a combination of potentiometric and spectroscopic techniques, the binding affinity of the three peptides models for Zn^{2+}. Moreover, we include in the study also Cu^{2+}, for comparison purposes, and to gain more insight into the metal coordination ability of this crucial ACE2 domain.

2. Results and discussion

2.1. Protonation equilibria

The deca-peptide Ac-L_{29}DKFNHEAED$_{38}$-NH_2 (P29-38) can be considered a H_6L ligand with six protonation constants in the pH range investigated (Table 1, Figure 3).

Preprints (www.preprints.org) | NOT PEER-REVIEWED | Posted: 4 May 2023 doi:10.20944/preprints202305.0226.v1

Table 1. Protonation constants at 298 K and I = 0.10 mol dm^{-3}, precision on the last significant figure in parentheses.

Ligand Species	Logβ	log$K$	Residue
$[HL]^{3-}$	10.21 (1)	10.21	Lys
$[H_2L]^{2-}$	17.05 (2)	6.84	His
$[H_3L]^{-}$	21.98 (2)	4.93	Glu
$[H_4L]$	26.36 (2)	4.38	Glu
$[H_5L]^{+}$	30.19 (2)	3.83	Asp
$[H_6L]^{2+}$	33.34 (2)	3.15	Asp

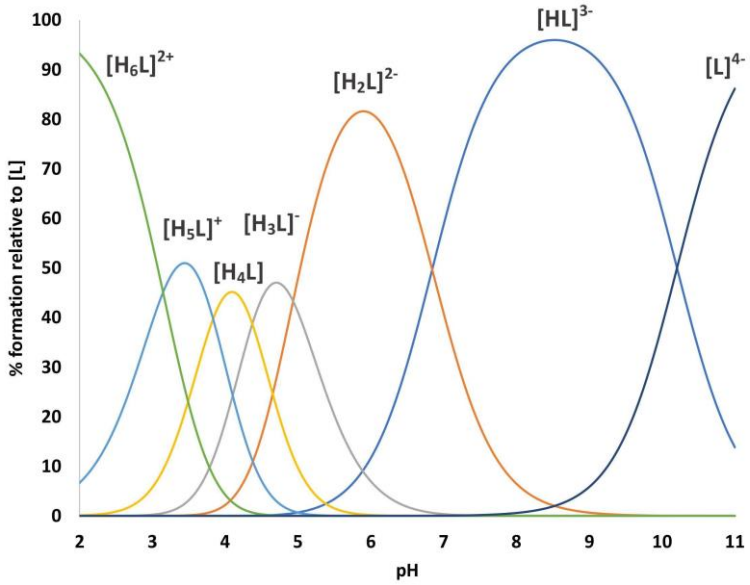

Figure 3. Representative distribution diagram for P29-38 peptide.

The first two pKa values (3.15 and 3.83) correspond to the deprotonation of the carboxylic group of Asp30 and Asp38 residues. The next two pKa values (4.38, 4.93) arise from the deprotonation of the Glu35 and Glu37. Potentiometric data cannot distinguish between the two Asp and Glu residues. The following two pKas (6.84 and 10.21) are the result of the deprotonation of His34 and Lys31 side-chains, in good agreement with the literature values of similar systems [26,27]. NMR spectra recorded for free peptide P29-38 in a wide range of values corroborated these deprotonation steps. Chemical shift changes following the increase of pH were detected for Asp and Glu nuclei at pH below 5, whereas for His residue large chemical shift changes have been detected from pH 6 to 7.4, and for Lys at pH > 10 (Figure S1). Unfortunately, both longer peptides, P23-42 and P19-42, were very poorly soluble in water, therefore it was not possible to perform potentiometric analysis. Consequently, their coordination ability towards Zn^{2+} and Cu^{2+} has been evaluated through NMR spectroscopy only.

Preprints (www.preprints.org) | NOT PEER-REVIEWED | Posted: 4 May 2023 doi:10.20944/preprints202305.0226.v1

2.2. Zinc(II) complexes

Peptide P29-38 forms 4 species with Zn(II) (Table 2, Figure 4).

Table 2. Complex-formation constants for Zn(II) complexes, at 298.2 K and I = 0.1 mol dm^{-3}. Precision on the last significant figure in parentheses.

Species	logβ	log$K$	Deprotonation	Coordination
[ZnH_2L]	20.34 (8)			Asp, Asp, Glu, (Glu)
[ZnHL]$^-$	14.55 (6)	5.79	His	(Asp), Asp, Glu, His
[$ZnLH_{-1}$]$^{3-}$	-1.50 (5)	8.025*2	2H_2O	(Asp), Asp, Glu, His
[$ZnLH_{-2}$]$^{4-}$	-11.42 (6)	9.92	Lys	(Asp), Asp, Glu, His

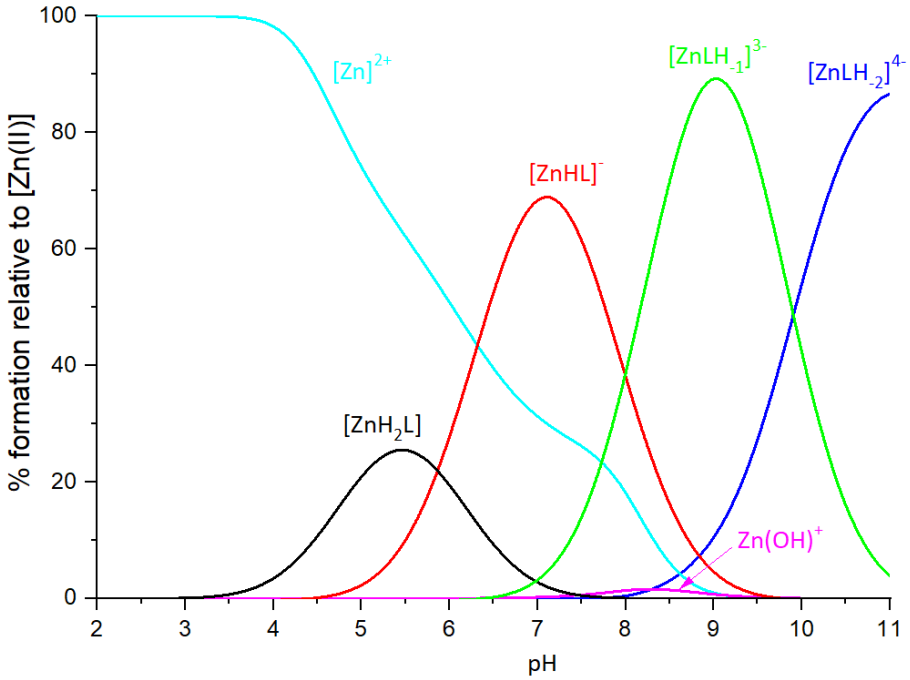

Figure 4. Representative distribution diagrams. $[Zn(II)]_{tot}$ = 0.4 mM; Zn(II)/L ratio =1 : 1.1.

The first species is [ZnH_2L], which starts from pH 3.5, and reaches only 28% of maximum of Zn^{2+} concentration in solution at pH 5.5. At this pH, all the carboxylic groups are almost completely deprotonated, while His34 and Lys31 residues are still protonated. The proposed coordination mode of Zn^{2+} could involve both aspartic residues Asp30 and Asp38, and one or both glutamate residues (Glu35 and/or Glu37). This species is soon replaced, starting from pH 4.5, by [ZnHL]$^-$ species which is present in solution till pH 9.5, with a maximum at pH 7 (about 75% of Zn^{2+} in solution). Zn^{2+} binding should involve, for this species, His34, Asp30, Asp38, and Glu37 residues. This coordination mode, through His34 bound to the metal ion, prevents, in fact, Glu35 coordination, as its sidechain is protruded toward the opposite side of the complex. The last two species are [$ZnLH_{-1}$]$^{3-}$ that starts forming from pH 6.5 till pH 11, with its maximum formation at pH 9, and [$ZnLH_{-2}$]$^{4-}$, that starts

Preprints (www.preprints.org) | NOT PEER-REVIEWED | Posted: 4 May 2023 doi:10.20944/preprints202305.0226.v1

forming from pH 8 with a maximum at pH 11. The deprotonation could involve, for the first species $[ZnLH_{-1}]^{3-}$, two water molecules and for $[ZnLH_{-2}]^{4-}$, the ammonium group of Lys31.

Nuclear magnetic resonance spectroscopy has been used to investigate the behavior of Zn^{2+} toward P29-38 in a wide range of pH as a supporting tool to the potentiometric results. The complete chemical shift assignment of proton and carbon nuclei at several pH values for the free peptide P29-38 has been performed with the help of complementary NMR techniques 2D ^{1}H-^{1}H TOCSY, ^{1}H-^{13}C-HSQC and ^{1}H-^{1}H ROESY. The Zn(II)-P29-38 system has been analyzed at pH 5, 5.5, 6, 7.4, 8, and 9. Figure 5 and 6 reports the comparison of free and Zn(II)-P29-38 system for a selected regions of TOCSY and HSQC spectra at pH 5 and 6, respectively. The red labeled signals refer to those perturbed after interaction with the metal ion.

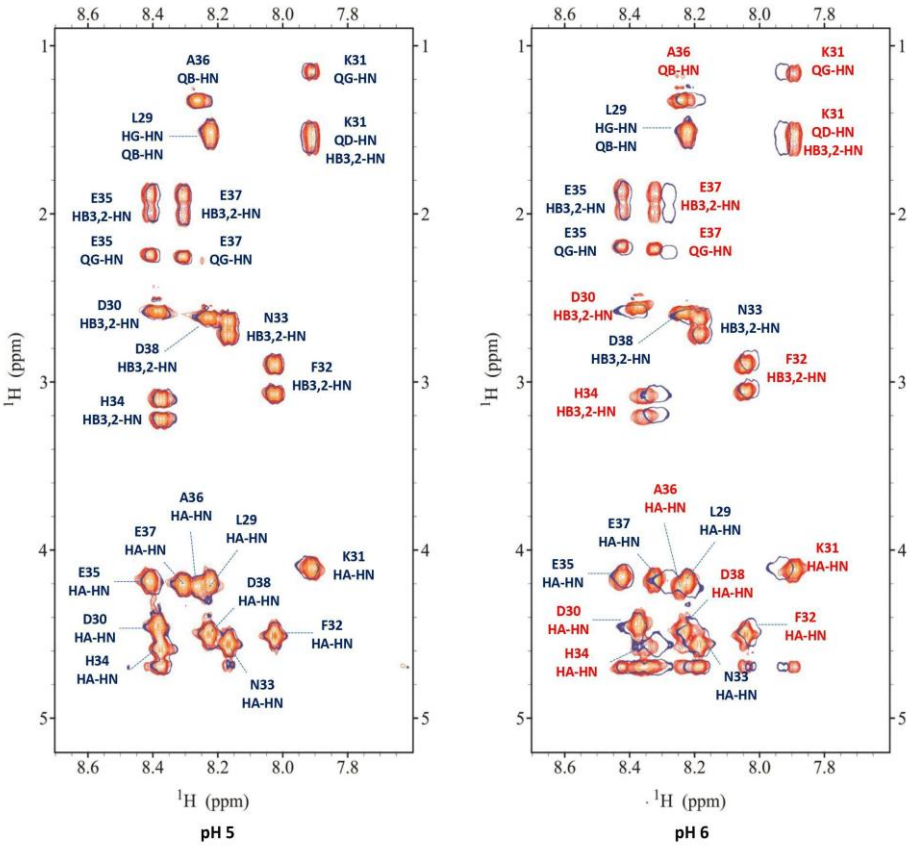

Figure 5. Superimposition of selected region of the ^{1}H-^{1}H TOCSY spectra for the free peptide P29-38 (orange) and Zn(II)-P29-38 system (blue contours) at pH 5 and 6.

Preprints (www.preprints.org) | NOT PEER-REVIEWED | Posted: 4 May 2023 doi:10.20944/preprints202305.0226.v1

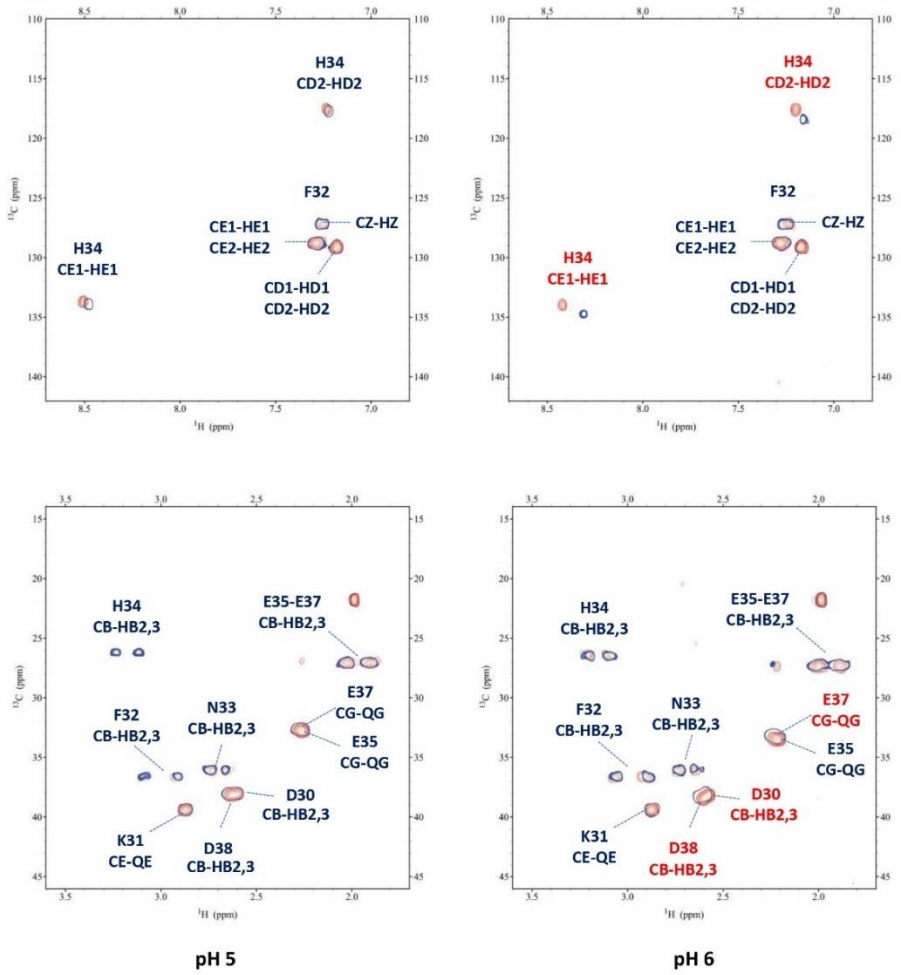

Figure 6. Superimposition of selected regions of the ^{1}H-^{13}C HSQC spectra for the free peptide P29-38 (orange) and Zn(II)-P29-38 system (blue contours) at pH 5 and 6.

Since the first species $[ZnH_2L]$ is present in very low concentration, spectra at pH 5 showed very little changes after Zn^{2+} addition. Increasing the pH up to 6 different perturbations can be observed both in the TOCSY and HSQC spectra. These perturbations are almost all related with the coordinating residues Asp30, Asp38 and Glu37 in agreement with the potentiometric previsions. The binding of Zn^{2+} to these residues also leads to selected perturbations on other nearby residues, such as Lys31, Phe32 and Ala36, which are indirectly affected by the complex formation since they experience a new electronic environment due to the subsequent conformational change of the peptide. Furthermore, His34 is also affected when the pH is increased, in agreement with its involvement in the metal binding with the following species $[ZnHL]^{-}$, that starts appearing from pH 4.5, while at pH 6 it reaches the same concentration in solution as the first species. The analysis of NMR spectra recorded at pH 7.4 gave us the full information regarding this following species. Figure 7 reports some significant examples of selective perturbations in the ^{1}H-^{13}C HSQC spectra of the residues involved in the binding with Zn^{2+} (Figure 7a). Furthermore, in Figure 7b the histogram relating to the variations of the chemical shifts between the Zn-P29-38 system and the free one for the H and C nuclei is reported. The scheme in Figure 7c gives a visual indication of the major perturbations that have been highlighted through the analysis of the NMR spectra at pH 7.4, and Figure 7d shows a proposed structural model of this system.

Preprints (www.preprints.org) | NOT PEER-REVIEWED | Posted: 4 May 2023 doi:10.20944/preprints202305.0226.v1

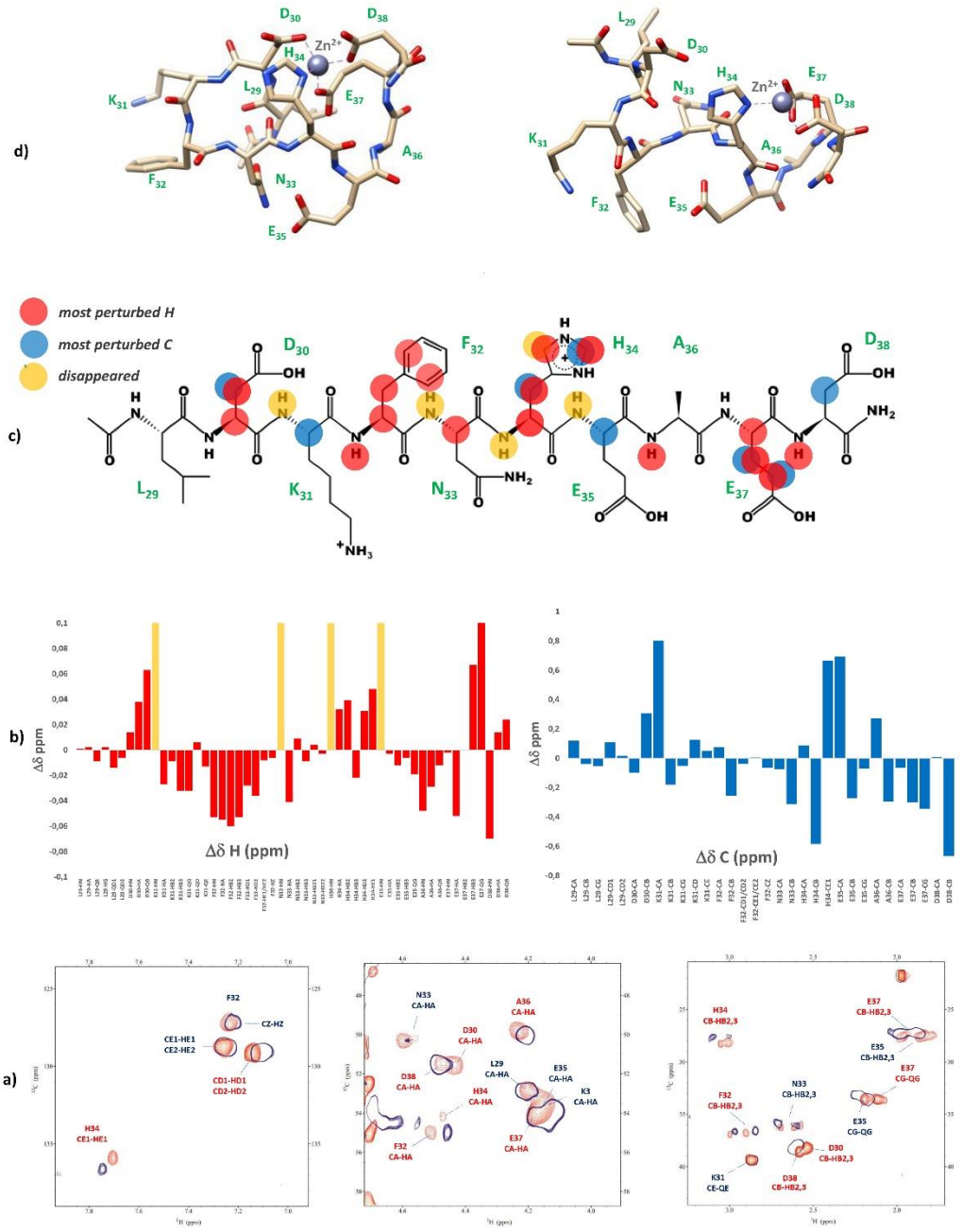

Figure 7. a) Superimposition of selected regions of the ^{1}H-^{13}C HSQC spectra for the free peptide P29-38 (orange) and Zn(II)-P29-38 system (blue contours) at pH 7.4; b) ^{1}H and ^{13}C chemical shift variations [Δδ = (Zn^{2+}-P29-38 system) – (P29-38 free)]; c) structural scheme of the peptide P29-38 upon Zn^{2+} binding with the most perturbed H and C nuclei highlighted; d) Structural models of the $[ZnHL]^{-1}$ species in a {(Asp), Asp, Glu, His} coordination mode.

Specific residues are perturbed in accordance with the potentiometric evaluation suggesting a {(Asp), Asp, Glu, His} coordination mode. In particular, the greatest variations of the chemical shift values are related to the nuclei in the side-chain of His34, Glu37, Asp30 and Asp38. NMR data confirm the Zn^{2+} binding to the imidazole ring of histidine. The trends of Δδ for Glu37 (QG>HB2/3>HA) and for Asp30, Asp38 (HB2/3>HA) indicate the involvement of metal binding through their carboxylic groups. Glu35 is not involved in the binding. Structural models have been built for this species and are depicted in Figure 7d. The Zn(II):P29-38 system at pH 8 and 9 resembles

Preprints (www.preprints.org) | NOT PEER-REVIEWED | Posted: 4 May 2023 doi:10.20944/preprints202305.0226.v1

that at pH 7.4 in agreement with the conclusion that the species $[ZnH_{-1}L]^{-3}$, maintains the same coordination sphere of $[ZnLH]^{-}$ (Figure S2).

Despite the low solubility, some useful information about the coordination ability of P23-42 peptide toward Zn^{2+} has been evaluated through NMR spectroscopy at pH 7. Figure 8 reports a comparison of 1D ^{1}H and a selection of ^{1}H-^{1}H TOCSY spectra at pH 7 between free peptide P23-42 and the Zn-bound system.

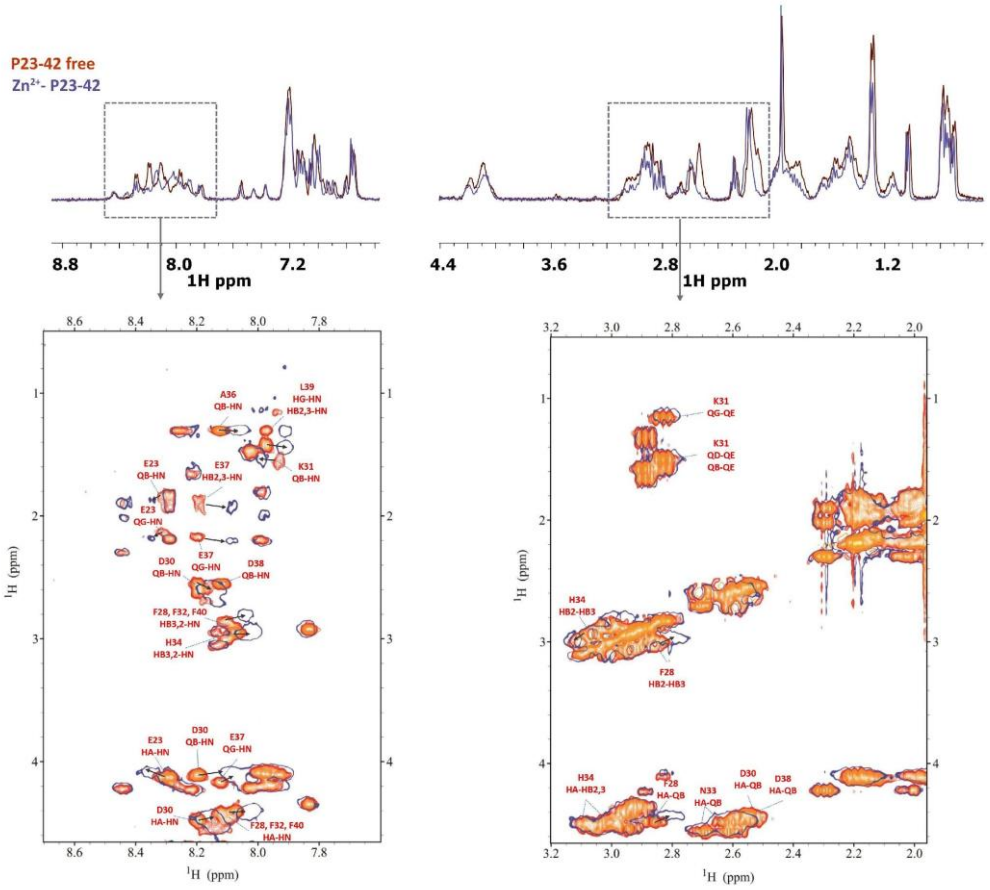

Figure 8. Comparison of ^{1}H spectra (up) and selection of ^{1}H-^{1}H TOCSY spectra (down) for the free peptide P23-42 (orange) and Zn(II)-P23-42 system (blue) at pH 7.0.

.

The main perturbations have been detected for Glu37, Asp30, followed by Asp38. Moreover, a few non-coordinating neighboring residues showed to undergo changes in the values of chemical shifts, i.e., Phe28, Lys31, Leu39, Phe40. Small variations have also been detected for the nuclei of His34. In particular, with the increase of the pH, it becomes clear how the imidazole protons of histidine are increasingly shifted, in accordance with the involvement of the imidazole ring in the binding with the metal ion at more basic conditions (Figure S3). From NMR analysis, the behavior of P23-42 peptide towards Zn^{2+} is similar to that observed for the shorter sequence P29-38. The anchoring site is centered in Glu-37 and Asp-38 and when the pH increases the involvement of His34 occurs. Moreover, together with Asp30, also Glu23 could play a secondary role in the metal interaction since its nuclei experienced selective perturbations. Peptide P19-42 has been revealed to be even less soluble than P23-42, however we were able to extract some information from NMR spectra. The longer peptide shows, broadly speaking, a coordination mode with Zn^{2+} very similar to that of the P23-42 peptide (Figure S4). The possibility of having additional information at basic pH was precluded by the precipitation of the Zn-system for both P23-42 and P19-42 peptides.

Preprints (www.preprints.org) | NOT PEER-REVIEWED | Posted: 4 May 2023 doi:10.20944/preprints202305.0226.v1

2.3. Copper(II) complexes

The complex-formation constants for the Cu(II)-P29-38 system are reported in Table 3, and the corresponding distribution diagrams are shown in Figure 9. UV-Vis and CD spectra at various pH values are given in Figure 10.

Table 3. Complex-formation constants for Cu(II) complexes, at 298.2 K and I = 0.1 mol dm^{-3}. Precision on the last significant figure in parentheses.

Species	logβ	log$K$	Deprotonation	Coordination
[CuH_2L]	20.78(5)			Asp, Asp, Glu, Glu
[CuHL]$^-$	16.01(3)	4.77	His	Asp, Asp, (Glu), His
[$CuLH_{-1}$]$^{3-}$	3.35(3)	2*6.33	amide, amide	His, $2N_{amide}$, (Asp or
[$CuLH_{-2}$]$^{4-}$	-4.17(4)	7.52	amide	His, $3N^-_{amide}$
[$CuLH_{-3}$]$^{5-}$	-13.09(5)	8.92	amide	$4N^-_{amide}$
[$CuLH_{-4}$]$^{6-}$	-24.29(5)	11.20	Lys	$4N^-_{amide}$

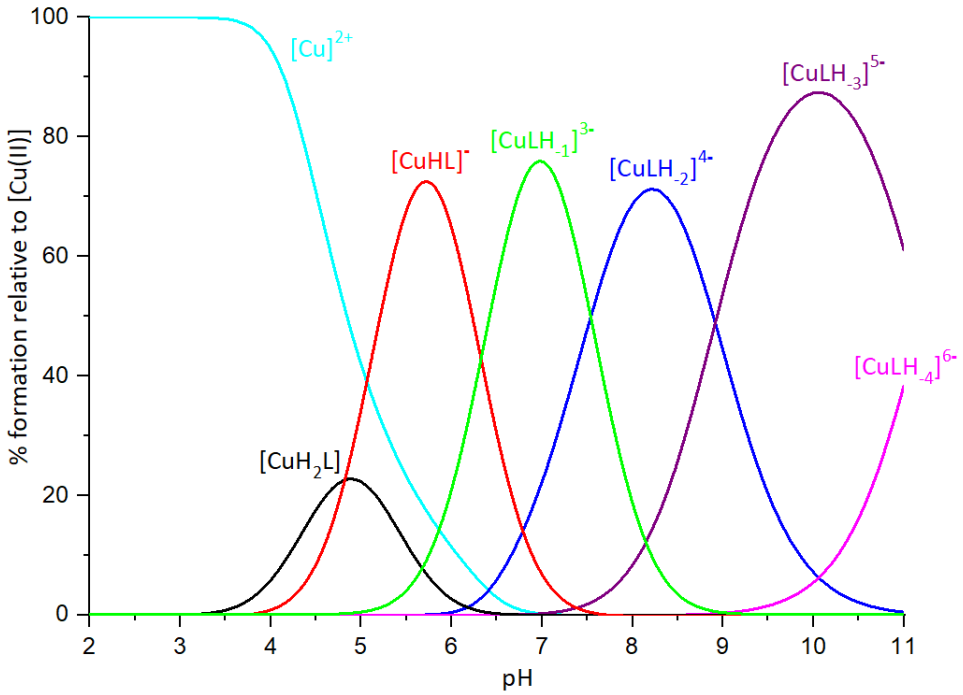

Figure 9. Representative distribution diagram. $[Cu(II)]_{tot}$ = 0.4 mM; Cu(II)/L ratio =1 : 1.1.

Preprints (www.preprints.org) | NOT PEER-REVIEWED | Posted: 4 May 2023 doi:10.20944/preprints202305.0226.v1

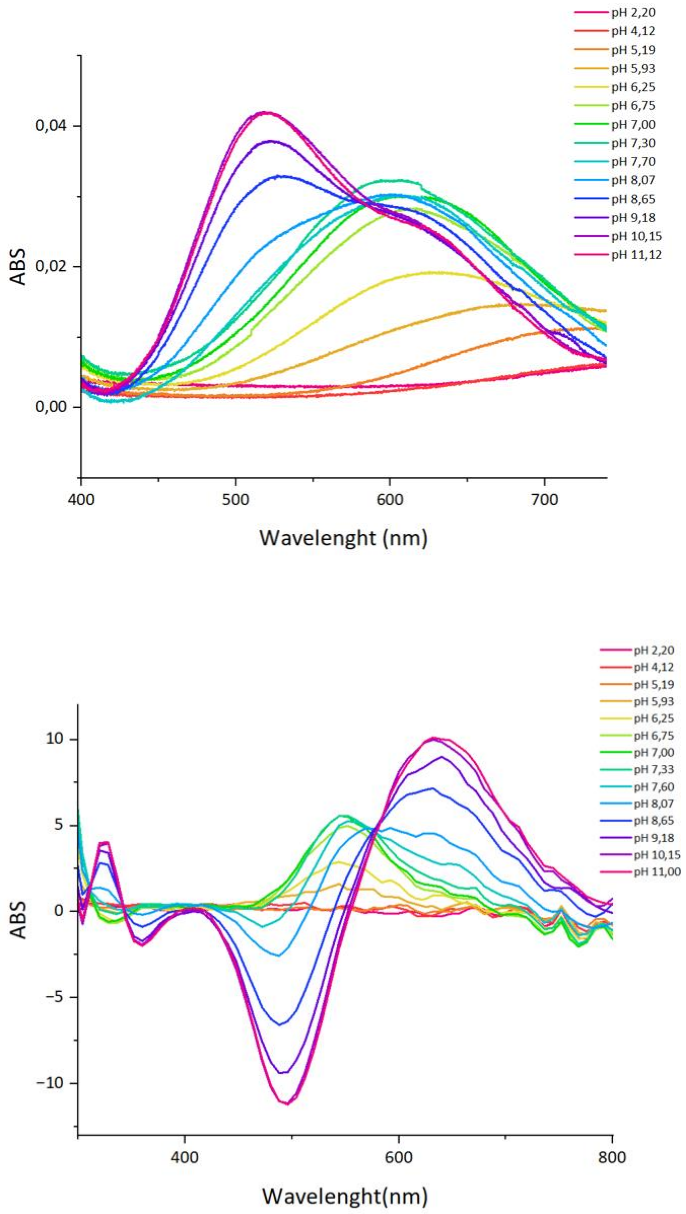

Figure 10. Cu(II)-P29-38 system. UV−vis spectra (up) and CD spectra (down) as a function of pH.

The formation of Cu(II) complexes with P29-38 begins at pH of about 3.5 with the [CuH_2L] species. Most likely the metal is bound by the carboxylic moieties of the two aspartate and two glutamate residues. This species has its maximum concentration at pH 4.5, but does not reach the 30% of the metal ion in solution. Consequently, due to its low abundance, the spectroscopic characteristic of this complexes is not accessible. Starting from pH 3.95, another proton is released, leading to the formation of $[CuHL]^-$ complex, which persists until pH 7.5, with a maximum at pH 5.5. This proton derives from the deprotonation of the His34 imidazole that is able to coordinate the copper ion at this pH. In the UV−Vis spectrum recorded at pH 5.19, the presence of a band with a maximum absorption at 715 nm suggests a single nitrogen atom in the metal ion coordination sphere. UV-Vis spectrum of $[CuHL]^-$ calculated by SPECFIT/32 software [28] based on pH-dependent spectra (Figure 10, Figure S5) shows a band characterized by λ_{max}= 720 nm, ε = 50 $M^{-1}cm^{-1}$ (Table 4), consistent with the experimental spectrum and the literature values for 1N {N_{Im}} Cu(II) d-d transition bands [29,30].

Preprints (www.preprints.org) | NOT PEER-REVIEWED | Posted: 4 May 2023 doi:10.20944/preprints202305.0226.v1

From CD spectroscopy it is possible to detect the ellipticity starting from pH 5.19 with a positive absorption band appearing in the range of 500-600 nm, which increase until pH 7.40, attributable to the interaction between His34 (ND2) and Cu^{2+}, as well as the presence of characteristic CD bands at 235 and 340 nm [N_{Im} → Cu(II) MLCT].

Table 4. UV-Vis spectroscopic parameters of nitrogen-coordinated complex forms in the Cu(II)-P29-38 system calculated by SPECFIT/32 software.

Complex form	Coordination	λ [nm]	ε [$M^{-1}·cm^{-1}$]
$[CuHL]^{-}$	1N {N_{Im}}	720	50
$[CuLH_{-1}]^{3-}$	3N {N_{Im}, 2N^{-}}	622	52
$[CuLH_{-2}]^{4-}$	4N {N_{Im}, 3N^{-}}	608	94
$[CuLH_{-3}]^{5-}$	4N {4N^{-}}	520	120

Due to the paramagnetic character of copper, NMR experiments for the Cu(II)-peptide system were performed by progressive addition of substoichiometric amounts of metal ions to the peptide solutions to avoid severe broadening of the signals. By following the selective relaxation effect experienced by nuclei closest to the paramagnetic Cu(II), it is possible to localize in the amino acid sequence the metal-binding donors and the changes undergone by the peptide upon interaction with the metal [26,31]. The NMR titration of P29-38 at pH 5.5 with increasing addition of sub stoichiometric amounts of Cu^{2+} is shown in Figure 11. In agreement with the proposed coordination mode {Asp, Asp, (Glu), His} the analysis of NMR spectra confirms the involvement of imidazole nitrogen of His34, and the carboxylate of Asp30, Asp38 and Glu37, since their signals were selectively and progressively reduced during Cu(II) titration. Comparison of ^{1}H-^{13}C HSQC for the free P29-38 and for Cu(II)-P29-38 system in the molar ratio of 0.01:1 and 0.1:1 highlighted, moreover, all the residues that were excluded from the relaxation effect of Cu(II), namely Leu29, Lys31 and Ala36, giving an indirect indication of their major distance from the paramagnetic ion (Figure S6).

Preprints (www.preprints.org) | NOT PEER-REVIEWED | Posted: 4 May 2023 doi:10.20944/preprints202305.0226.v1

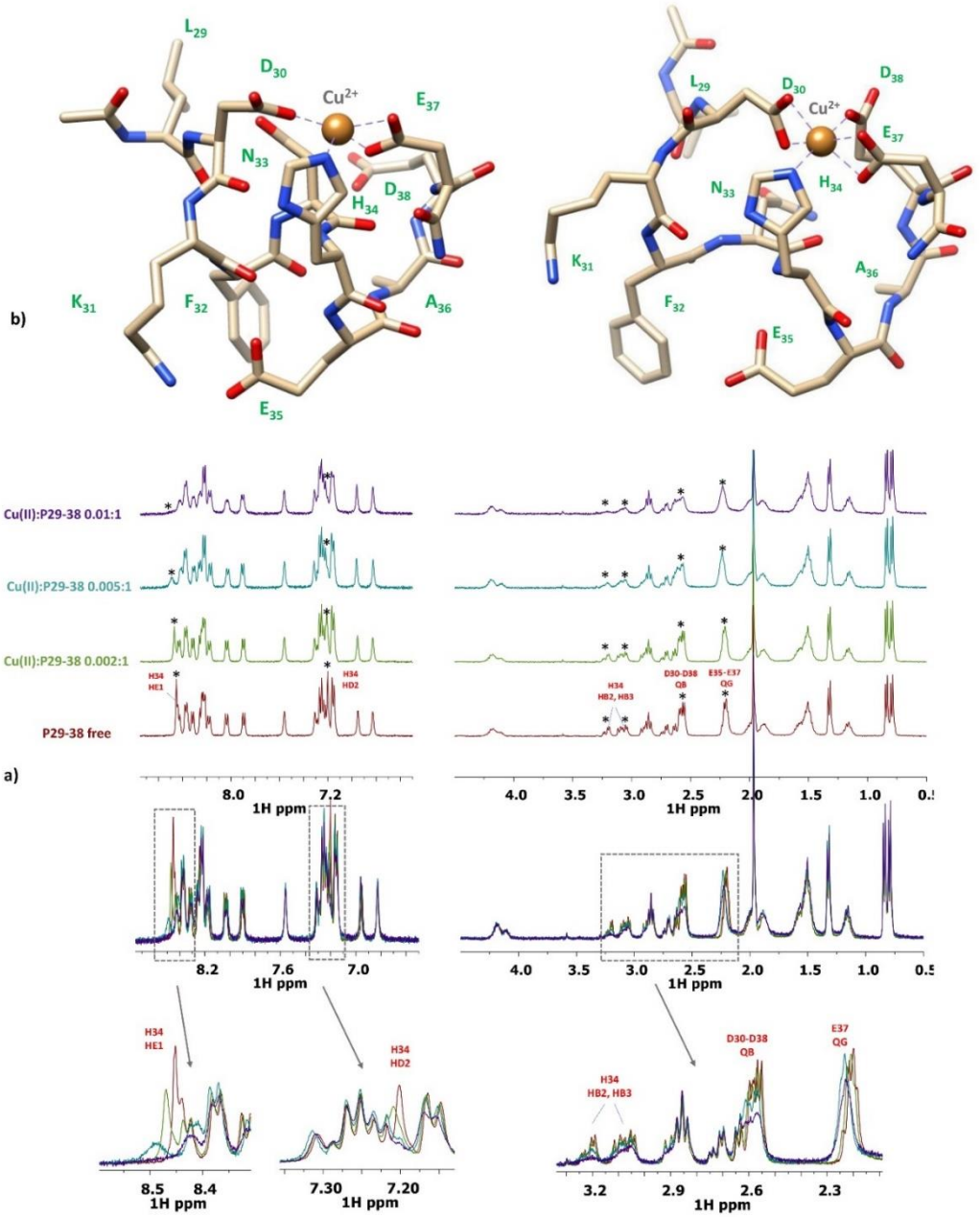

Figure 11. a) Comparison of ^{1}H spectra of P29-38 with increasing addition of Cu^{2+} at pH 5.5; b) Structural models of the $[CuHL]^{-1}$ species in a {Asp, Asp, (Glu), His} coordination mode.

The next species $[CuLH_{-1}]^{3-}$ starts appearing from pH 5 and derives from two consecutives deprotonations that can be assigned to two backbone amide nitrogen. The average corresponding pK_{step} values of 6.33 are compatible with this hypothesis. In fact, once anchored to the peptide through a His residue, Cu^{2+} is able to displace the amide protons through a cooperative effect which facilitates the coordination of the other amide nitrogen as the pH increases. Starting from pH 5.93, UV-Vis absorption band starts shifting towards the shorter wavelength, thus reflecting the formation of this new complex form, $[CuLH_{-1}]^{3-}$, derived from two consecutives backbone amide nitrogen deprotonations. In this form, the coordination of the copper ion is most probably 3N {N_{Im}, $2N^{-}$}, λ_{max} = 622 nm, ε = 52 $M^{-1}cm^{-1}$ (Table 4). The presence of $[CuLH_{-1}]^{3-}$ is also reflected in CD spectra by the formation of the band at 540 nm (d-d transition) and 310 nm ($N^{-} \rightarrow Cu(II)$ charge transfer transition), indicating the involvement of amides in the metal coordination [32,33].

Preprints (www.preprints.org) | NOT PEER-REVIEWED | Posted: 4 May 2023 doi:10.20944/preprints202305.0226.v1

NMR titration of P29-38 with increasing addition of substoichiometric amount of Cu^{2+} has also been performed at pH 7.4. Figure 12 (and Figure S7) reports the results of this NMR study.

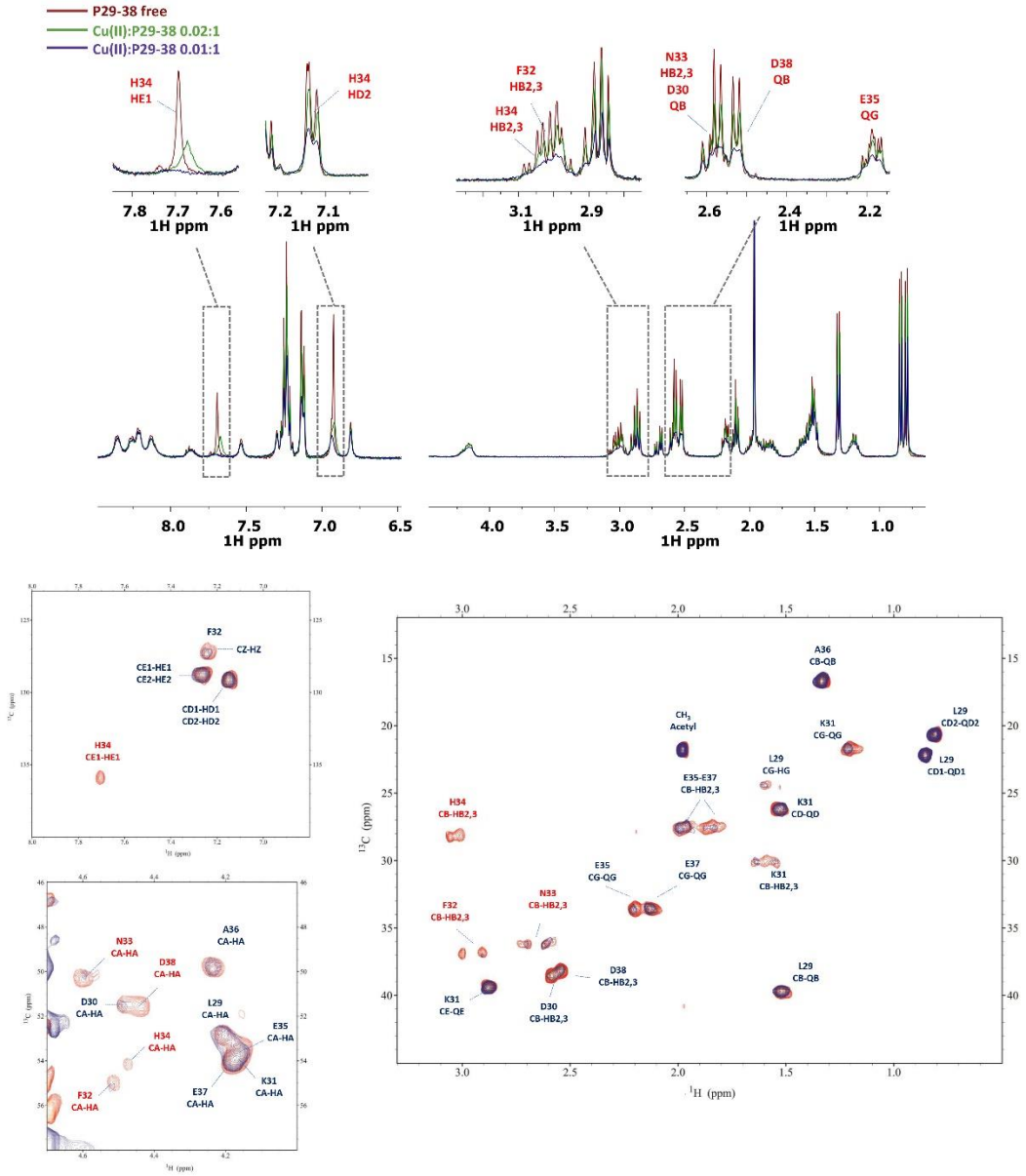

Figure 12. (up) Comparison of ^{1}H spectra of P29-38 with increasing addition of Cu^{2+} at pH 7.4; (down) comparison of ^{1}H-^{13}C HSQC spectra of P29-38 free (orange) and Cu(II)-P29-38 at 0.1:1 molar ratio (blue) at pH 7.4.

The NMR study performed at pH 7.4, still clearly evidenced the involvement of His34 in the coordination sphere of Cu(II). The imidazole proton HD2 and HE1 experienced a severe line broadening together with HB2-HB3 in its side-chain. Other residues influenced are the adjacent Asn33 and Phe32 (in particular in their alpha and beta nuclei) which experienced a signal disappearance for the effect of their proximity to the paramagnetic metal ion. It is evident from the spectra that the participation of acidic residues in the complex formation is diminishing, in accordance with the coordination mode change involving nitrogen amides. As the pH increases, another backbone amide deprotonates, with the p*K* value of 7.52. It is the $[CuLH_{-2}]^{4-}$ form, characterized by 4N {N_{Im}, $3N^{-}$} coordination. Due to the equilibrium in solution of 3N and 4N

Preprints (www.preprints.org) | NOT PEER-REVIEWED | Posted: 4 May 2023 doi:10.20944/preprints202305.0226.v1

coordination forms, it is difficult to clearly discern between their spectroscopic bands. In general, the 3N Cu(II) coordination in $[CuLH_{-1}]^{3-}$ form can be clearly seen at pH = 6.25, with λ_{max} = 622 nm. Under higher pH, up to 7.70, the band moves to shorter wavelength of about 608 nm and its intensity rises, as the third amide enters the coordination sphere in $[CuLH_{-2}]^{4-}$. The bands calculated by SPECFIT/32 are characterized by λ_{max} = 622 nm (ε = 52 $M^{-1}cm^{-1}$) and λ_{max} = 608 nm (ε = 94 $M^{-1}cm^{-1}$) for 3N and 4N forms, respectively (Table 4, Figure S5). Similar behavior is also reflected in CD spectra, with the increasing intensity of the band at about 540 nm, rising up to pH = 7.60.

The next complex form, $[CuLH_{-3}]^{5-}$, is present in the solution already from pH of about 7, with its maximum concentration at pH about 10. This form derives from the deprotonation of the fourth backbone amide nitrogen, with the p*K* value of 8.92. The imidazole nitrogen, bound to the Cu(II) already from the pH of about 4, is most probably displaced by the amide nitrogen, resulting in 4N $\{4N^-\}$ coordination mode. This can be clearly seen in both UV- Vis and CD spectroscopies. In the UV-Vis spectrum recorded at pH = 8.07, another component of the band starts rising at about 520 nm, reflecting the equilibrium in the solution between the $[CuLH_{-2}]^{4-}$ 4N $\{N_{Im}, 3N^-\}$ and $[CuLH_{-3}]^{5-}$ 4N $\{4N^-\}$ forms. The UV- Vis spectrum calculated for the $[CuLH_{-3}]^{5-}$ with λ_{max} = 520 nm (ε = 120 $M^{-1}cm^{-1}$) (Table 4, Figure S5) reflects the presence of $4N^-$ form, consistent with the literature values [29,34]. In the CD spectrum recorded at the same pH, a drastic change compared to the previous spectra can be seen, with new bands at 500 nm and 650 nm that start appearing, indicating the altered coordination of the metal ion. Indeed, these d-d transition bands are characteristic for the square planar, amide involving complexes [35]. With the increasing pH up to about 11, the intensity of these bands increases, reflecting the rising concentration of the $[CuLH_{-3}]^{5-}$ form, shifting the equilibrium towards the $4N^-$ coordination mode. The last complex form, $[CuLH_{-4}]^{6-}$, is a result of the deprotonation of the non-binding ε- amino side- chain group of the lysine residue, with the p*K* value of 11.20.

Since at high pH values, in the Cu(II)-systems we detected a severe line broadening in the NMR spectra, which prevented the detailed characterization of the species in the $[N_{Im}, 3N^-_{amide}]$ coordination mode, we decided to probe Cu^{2+} binding to the P29-38 peptide using diamagnetic Ni^{2+}. In terminally blocked peptides containing histidine residue from the third position onwards, Ni^{2+} forms diamagnetic, low-spin, square planar complexes at appropriately high pH. The imidazole nitrogen of histidine serves as an anchoring site and once bound to it, Ni^{2+} is able (like Cu^{2+}) to deprotonate and bind three additional amide nitrogen from the backbone, thus completing the coordination sphere of $[N_{Im}, 3N^-_{amide}]$ with simultaneous formation of three fused chelated rings and the saturation of the coordination plane [36,37]. Therefore, Ni^{2+} could be used as Cu^{2+} probe since it is able to replace it in the equivalent square planar complexes, but forming low-spin diamagnetic species, which are more easily investigated by NMR [38,39]. Figure 13 reported the metal titration at pH 10.6, by addition of increasing amounts of Ni(II) ions, up to a 0.8 : 1, Ni(II):P29-38 molar ratio. Figure 14 shows the histograms related to the ^1H and ^{13}C chemical shift variations, the structural scheme of the peptide P29-38 with the most perturbed H and C nuclei and the structural model proposed of the corresponding Ni^{2+} species.

Preprints (www.preprints.org) | NOT PEER-REVIEWED | Posted: 4 May 2023 doi:10.20944/preprints202305.0226.v1

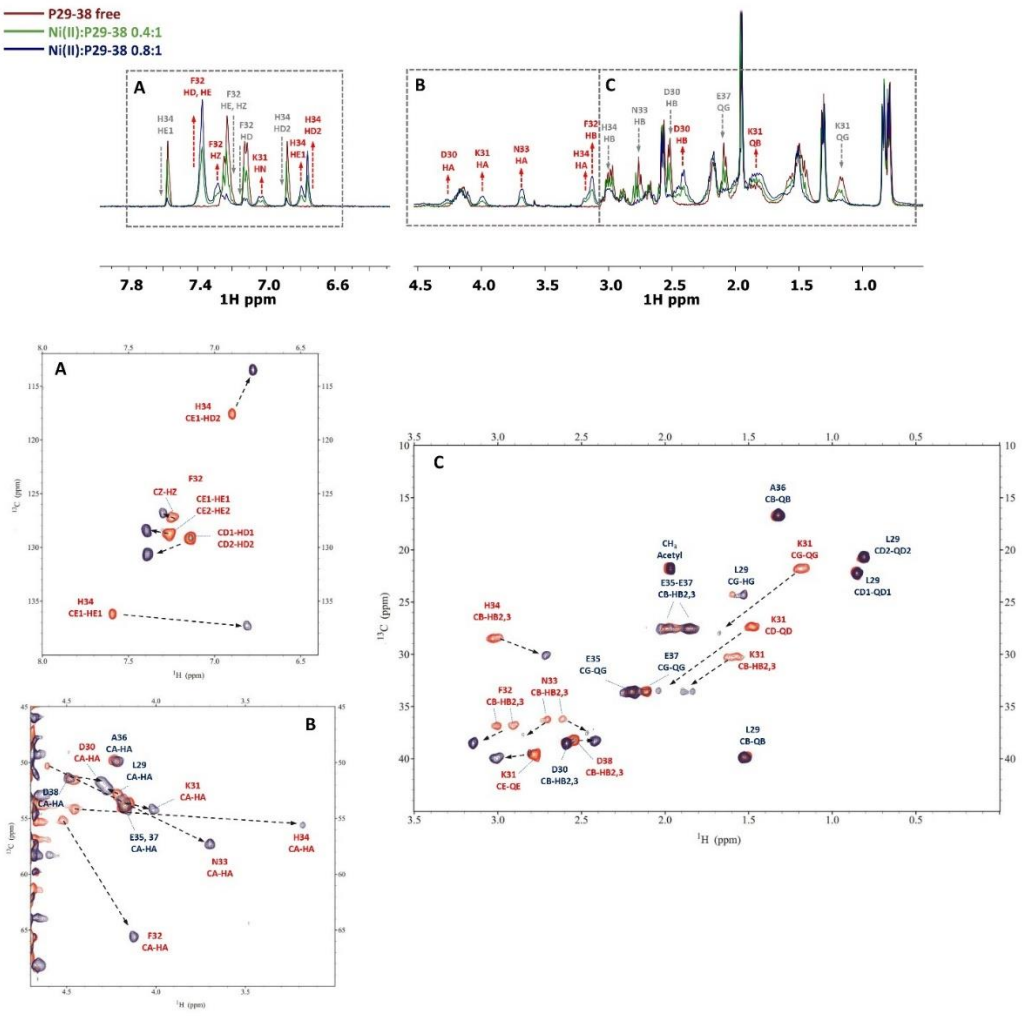

Figure 13. (up) Comparison of ^{1}H spectra of P29-38 with increasing addition of Ni^{2+} at pH 10.6. Gray arrows indicate signals that gradually decrease in intensity while red arrows refer to new signals that gradually appear upon addition of Ni^{2+}; (down) comparison of ^{1}H-^{13}C HSQC spectra of P29-38 free (orange) and Ni(II)-P29-38 at 0.8:1 molar ratio (blue) at pH 10.6; the black arrows indicate the new positions of the NMR signals following the addition of Ni^{2+}.

Preprints (www.preprints.org) | NOT PEER-REVIEWED | Posted: 4 May 2023 doi:10.20944/preprints202305.0226.v1

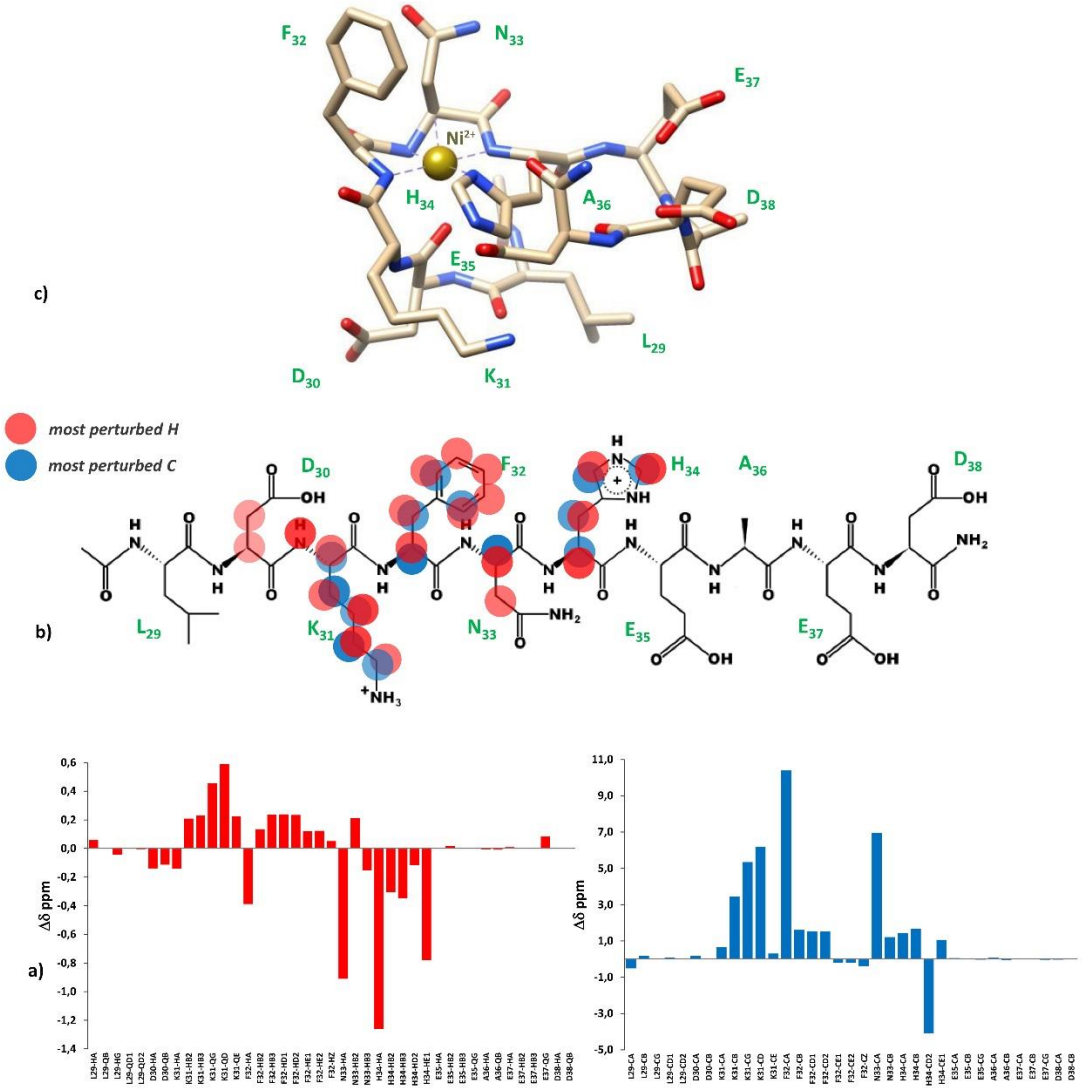

Figure 14. a) ^{1}H and ^{13}C chemical shift variations [Δδ = (Ni^{2+}-P29-38 system) – (P29-38 free)]; c) structural scheme of the peptide P29-38 with the most perturbed H and C nuclei highlighted upon Ni^{2+} binding; d) Structural model of the Ni^{2+} species in a [N_{Im}, $3N^{-}_{amide}$] coordination mode.

Several changes were detected in the NMR signals of peptide upon nickel addition. The diamagnetic complex formation is confirmed by the shift of numerous signals related to the specific residues His34, Asn33, Phe32 and Lys31. The involvement of His34 is immediately recognized by the gradual disappearing of the relative resonances of the imidazole HD2 and HE1 and aliphatic HA, HB signals in the free peptide and the simultaneous appearance of a new set of peaks related to the metal bound form in slow exchange on the chemical shift time-scale. In particular, the chemical shift differences Δδ between the imidazole aromatic proton from the bound and free state, greater for HE1 respect to HD2 (Δδ HE1 = 0.783 ppm > Δδ HD2 = 0.121 ppm) give a clear indication of the metal bound to the adjacent imidazole nitrogen ND1 (Figure 13a and 14 a). All the His34 protons are shielded according to the increased electron density. The chemical shift changes are more pronounced for the residues taking part to metal coordination: His34, Asn33, Phe32 and Lys31. The major variations, according to the formation of a low-spin diamagnetic complex (square-planar, or five-coordinate square-pyramidal) are related to the HA protons, which are greatly shielded due to the influence of an increased electron density upon amide deprotonation (Figure 13b and 14). The trend of changes

Preprints (www.preprints.org) | NOT PEER-REVIEWED | Posted: 4 May 2023 doi:10.20944/preprints202305.0226.v1

with Δδ HA > HB and Δδ CA > CB is coherent with a coordination mode involving the backbone nitrogen amide of His34, Asn33 and Phe32. The HB2 and HB3 protons of Phe32 and Asn33 exhibit different electronic environment as one is up-field and the other is down-field shifted. This behavior is most likely due to a blocked position of the Phe32 and Asn33 side-chains above the complex which causes only part of the side-chain to be shielded (Figure 13c and 14). ROE cross-correlations have in fact been identified between phenolic HD proton of Phe32 and the imidazole HE1 proton of His34. Additional ROEs have been identified between neighboring nuclei and in particular between the side-chain protons of Phe32 and Asn33, that confirm their relative position in the same side of the coordination plane. Similarly, the side-chain protons of Lys31 are strongly deshielded, due to a blocked conformation in the opposite side respect to Asn33 and Phe32 side-chains. A more rigid spatial conformation of Lys31, under the plane of the complex, is confirmed by the fact that during the Ni^{2+} titration the amide proton HN of Lys31 showed ROE correlations with the HA proton of Asp30 and its HA with the HE1 and HD2 protons of His34. Interestingly, this labile proton HN reappears after the addition of Ni^{2+}, and it is probably blocked, as if it were involved in a hydrogen bond. The blocked conformation of the backbone relate to the position of Asp30 could explain, moreover, the possibility of a five-coordinate square-pyramidal coordination trough the carbonyl of Asp30 interacting with the metal in axial position under the plane of the complex, as suggested by the model depicted in Figure 14c. To verify if Ni^{2+} was a good probe of Cu^{2+} we have done a NMR competition studies, by titrating the diamagnetic Ni(II):P29-38 system (0.8:1 molar ratio) with increasing substoichiometric amount of paramagnetic Cu^{2+}. The already shifted signals due to Ni(II) binding, related to the residues taking part of the metal complexation, selectively disappeared during the titration, an indication that Cu^{2+} ions were able to displace and substitute Ni^{2+} ions in the same coordination site (Fig S8). Moreover, the addition of Cu^{2+} to the Ni(II):P29-38 system showed further clues on the involvement of the fourth amide N^- in the complexation, since the already citated amide HN signal of Lys31 disappears due to its deprotonation and subsequent coordination with the metal ion. The involvement of Lys31 is furthermore evidenced by the disappearing or by the severe lowering of its spin system signals, as an indication of its new location in the proximity of the paramagnetic ion. A proposed structural model of the Cu(II):P29-38 in a $4N^-_{amide}$ coordination sphere is depicted in Figure 15.

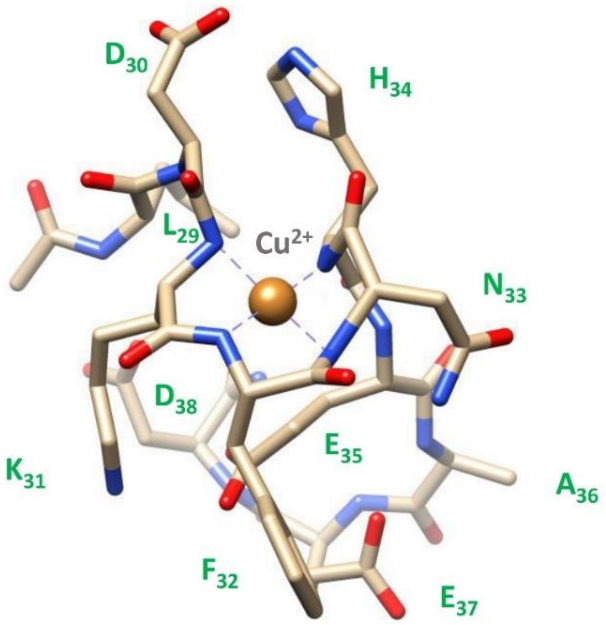

Figure 15. Structural model of the Cu^{2+} species in a [$4N^-_{amide}$] coordination mode.

Preprints (www.preprints.org) | NOT PEER-REVIEWED | Posted: 4 May 2023 doi:10.20944/preprints202305.0226.v1

The NMR study of the longer peptides P23-42 and P19-42 has provided some evidence on the coordination preferences of Cu^{2+}. At pH 7 both Cu(II)-P23-42 and Cu(II)-P19-42 systems showed a selective disappearance of the signals related to His-34, Asp-30 and Asp-38 (Figure S9 and S10) and when pH was set to 8 the involvement of Glu-35 and Glu-37 appeared more clearer. At higher pH the concomitant effect of excessive line-broadening and poor solubility prevented better characterization of Cu(II)-systems for both systems P23-42 and P19-42 peptides. However, to obtain further information on the species that form at high pH values, we used Ni^{2+} as a Cu^{2+} probe also for the longer peptide P19-42. The results are strikingly similar to those obtained for the shorter peptide P29-38. In fact, the titration at pH 10.6 led to obtain a system in which Ni forms a diamagnetic planar complex involving, similarly to peptide P29-38, not only the same coordinating residue of His34 (N_{im}, N^-), Asn33 (N^-), Phe32 (N^-), (Figure 16, S11) but also showing almost identical chemical shift differences (Δδ ppm) between the two systems (Figure 17). As in the case of minimal model P29-38 the labile proton HN of Lys31 reappears after addition of Ni^{2+} and also several ROEs that were identified for the Ni^{2+}-P29-38 system have been confirmed for Ni^{2+}-P19-42 system, and in particular: Asp30HA-Lys31HN, Lys31HA-His34HD2, Lys31HA-His34HE1, Phe32HB2-His34HD2, Asn33HB2-Phe32HD, Asn33HB3-Phe32HD, His34HE1-Phe32HD, which were related with the blocked conformation of side-chain Phe32 and Asn33 above and Lys31 under the plane of the complex.

The competition study was also conducted for the longest peptide with increasing amounts of Cu^{2+}, added in the Ni(II)-P19-42 system, at pH 10.6. Exactly, as in the case of the shorter peptide P29-38, the signals related to Ni^{2+} binding and involving His34, Asn33 and Phe32, which play the main role in metal complexation, selectively disappeared following the substitution of the paramagnetic Cu^{2+} ion with the diamagnetic one Ni^{2+}, in an identical coordination sphere around the metal ion (Fig S12). The involvement of nitrogen amide of Lys31 in the $4N^-$ coordination mode, is evidenced, like before, by the disappearance of its HN spin-system.

Preprints (www.preprints.org) | NOT PEER-REVIEWED | Posted: 4 May 2023 doi:10.20944/preprints202305.0226.v1

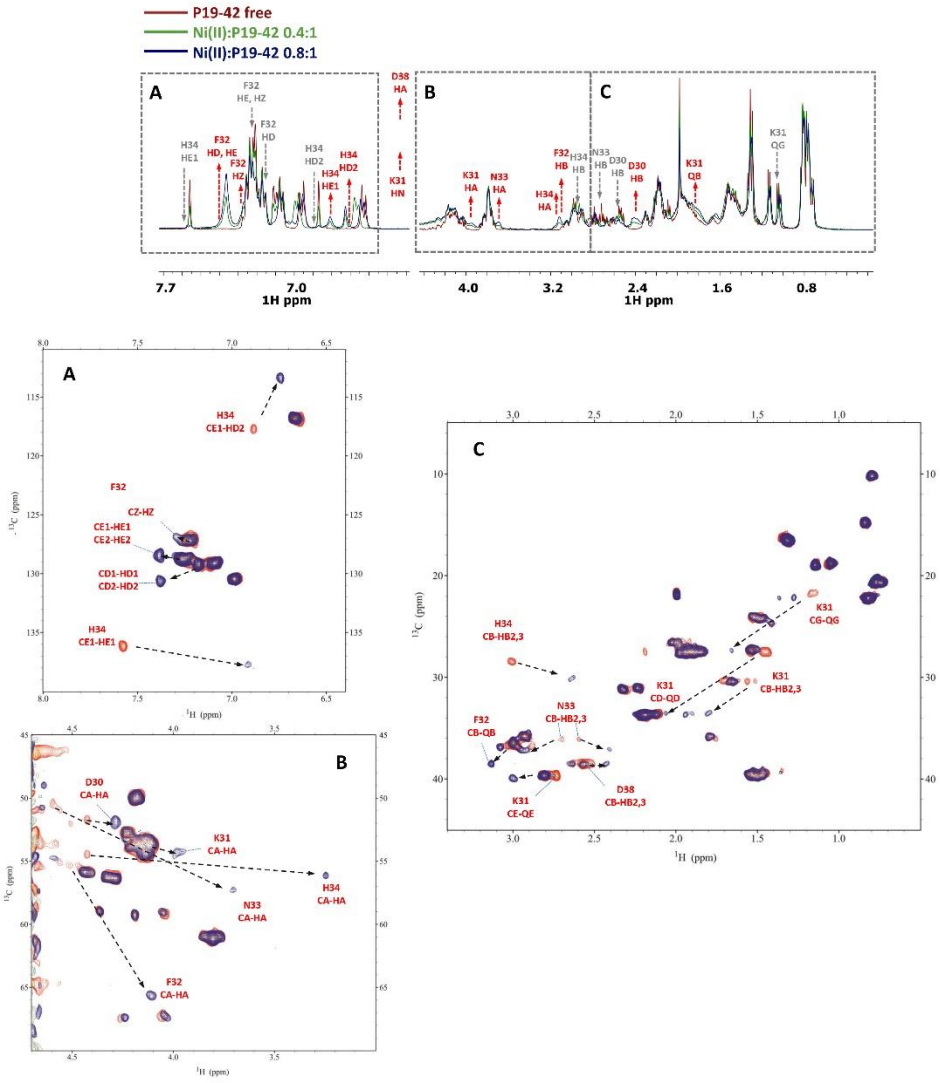

Figure 16. (up) Comparison of ^{1}H spectra of P19-42 with increasing amounts of Ni^{2+} at pH 10.6. Gray arrows indicate signals that gradually decrease in intensity while red arrows refer to new signals that gradually appear upon addition of Ni^{2+}; (down) comparison of ^{1}H-^{13}C HSQC spectra of P19-42 free (orange) and Ni(II)-P19-42 at 0.8:1 molar ratio (blue) at pH 10.6; the black arrows indicate the new positions of the NMR signals following the addition of Ni^{2+}.

Preprints (www.preprints.org) | NOT PEER-REVIEWED | Posted: 4 May 2023 doi:10.20944/preprints202305.0226.v1

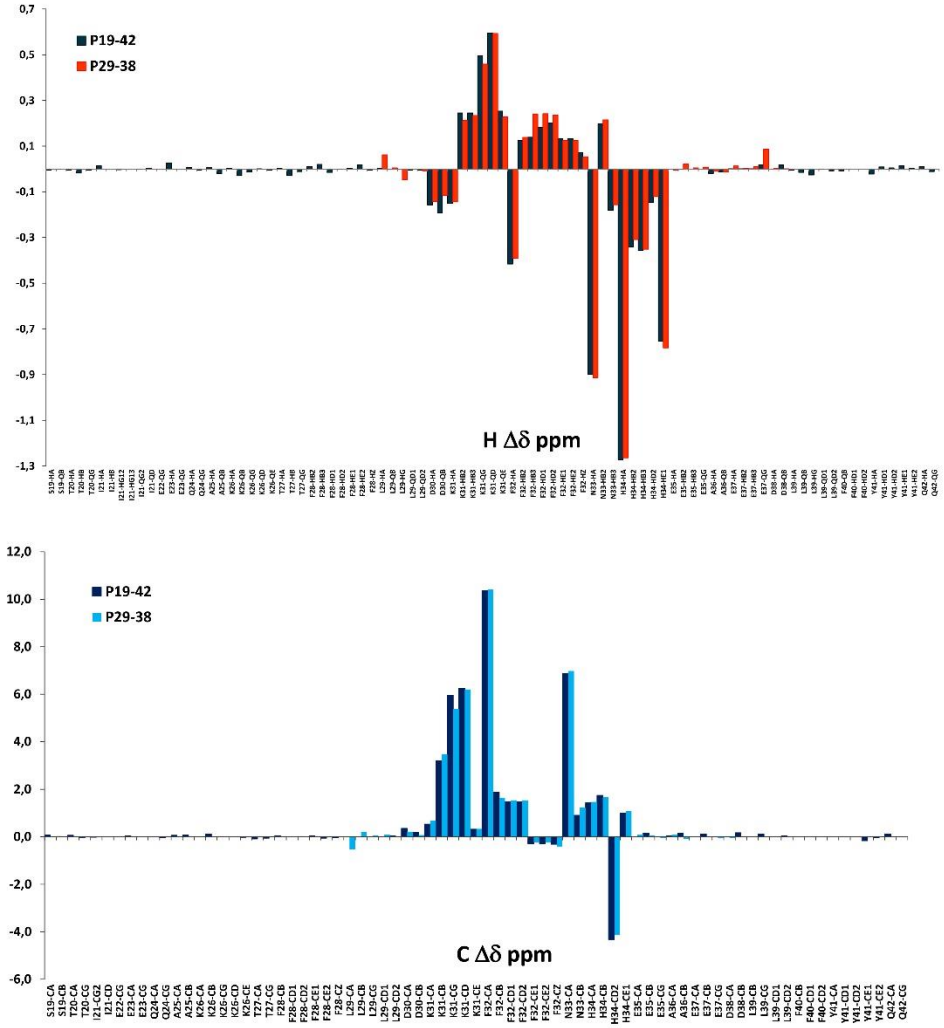

Figure 17. Comparison of ^{1}H and ^{13}C chemical shift variations for P19-42 and P29-38 peptides upon Ni^{2+} coordination.

2.4. Competition diagrams

The competition plot between P29-38 and Zn(II) and Cu(II) ions illustrates (Figure 18) the complex formation in a hypothetical situation, when equimolar amounts of all reagents are mixed in the solution. Up to pH of about 2.8 almost all of the ligand exists in uncomplexed form. From pH = 3 the beginning of complexation can be clearly seen, with copper complexes dominating over zinc complexes already in these acidic conditions, a behavior which persists all the way up to pH = 11. Cu(II) complexes quickly reach over 60% of the ligand molecules bound at pH of about 4. Around this pH, the maximum concentration of Zn(II) complexes is also achieved, reflecting the start of deprotonation and binding of histidine H34 by Zn^{2+}. With the increasing pH, Zn(II) complexes concentration starts to drop down, with less than 5% percent of the ligand bound at pH = 7. Quite contrary, a rise in Cu(II) complexes concentration can be seen, reflecting the increasing involvement of nitrogen ligands in copper binding, such as the histidine residue and amide groups. Reaching the 90% of the ligand bound already at pH = 6.50, Cu(II) complexes clearly dominate over those of Zn(II), whose coordination sphere remains unchanged in the basic pH range. The behavior observed in the competition plot of P29-38 with Zn(II) and Cu(II) is in agreement with the Irving-Williams series, in which the stability of divalent copper complexes is higher than those of divalent zinc complexes [40].

Preprints (www.preprints.org) | NOT PEER-REVIEWED | Posted: 4 May 2023 doi:10.20944/preprints202305.0226.v1

The results of this experiment remain valid for a hypothetical situation when equimolar amounts of all reagents are used. In human cells the situation can be completely reversed, since the relative concentrations of free copper and zinc in plasma are not the same, being about 10^{-18}–10^{-13} M for copper and around 10^{-9} for zinc [41,42].

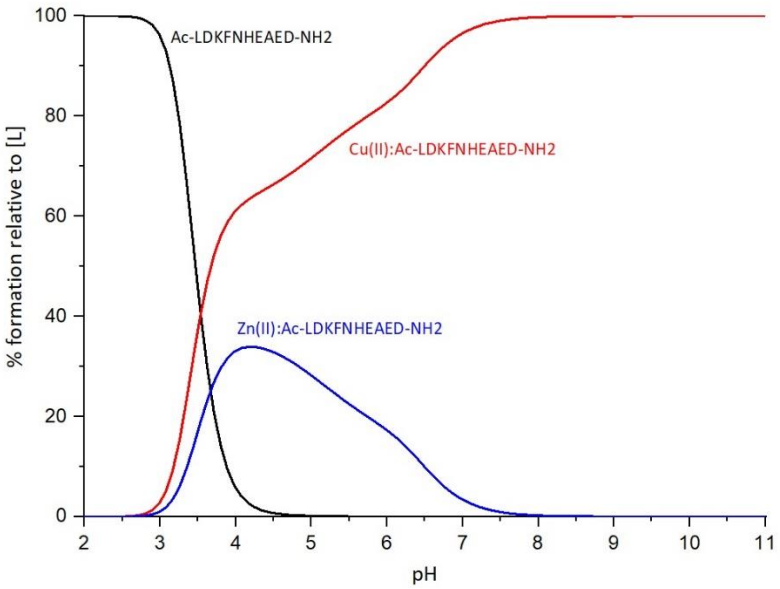

Figure 18. Competition plot, depicting a hypothetical situation in which all reagents are mixed in equimolar.

3. Materials and Methods

3.1. Peptide synthesis

P29-38 (Ac-LDKFNHEAED-NH_2), P23-42 (Ac-EQAKTFL$_{29}$DKFNHEAEDLFYQ-NH_2), and P19-42 (Ac-STIEEQAKTFLDKFNHEAEDLFYQ-NH_2) peptides were purchased from Biomatik Corporation, Ontario (CA). All peptides have a purity > 97%. All of the chemicals used in this work were purchased from Sigma-Aldrich and used without any further purification.

3.2. Potentiometric measurements

All the potentiometric data were calculated from two titration experiments carried out over the pH range 2.0–11.0 at 298 K in 0.1 M $NaClO_4$ using a total volume of 2 mL. Metrohm Titrando 905 titrator connected to Dosino 800 dosing system and pH electrode InLab Semi-Micro (Mettler-Toledo) were used to carry out the experiments. The electrode was calibrated every day for the hydrogen ion concentration by titrating 2 mL of 4 mM perchloric acid with sodium hydroxide. All potentiometric measurements were performed under an argon atmosphere. Purities and exact concentrations of ligand solutions were determined by the Gran method [43]. Ligand concentration was 0.5 mM, metal to ligand molar ratio was 1: 1.1. HYPERQUAD 2008 [44] and SUPERQUAD [45] programs were used to calculate the stability constants. Standard deviations were computed using HYPERQUAD 2008 and they refer to random errors only. Cu(II) and Zn(II) hydrolysis constants were taken into account for the calculations of stability constants of complexes. The hydrolysis constants for zero ionic strength were taken from the "Hydrolysis of Metal Cations" by Brown and Ekberg [46] and calculated to 0.1 M ionic strength with the formula proposed by Baes and Mesmer in "The Hydrolysis

Preprints (www.preprints.org) | NOT PEER-REVIEWED | Posted: 4 May 2023 doi:10.20944/preprints202305.0226.v1

of Cations" [47]. Metal hydrolysis constants are collected in Table S1 .The competition and speciation diagrams were created using HYSS software [48].

3.3. UV-Vis and CD measurements

Absorption spectra were recorded in the 240–800 nm range on a Jasco J-1500 spectropolarimeter (CD) and on a Jasco V-750 spectrophotometer (UV-Vis); solutions were of similar concentrations to those used in the potentiometric studies; ligand concentration was 0.5×10^{-3} mol dm^{-3} and the tested Cu(II) : ligand molar ratio was 1 : 1. Absorptivities (ε, M^{-1} cm^{-1}) were calculated at the pH value of maximum concentration of the considered species, as indicated by the potentiometric distribution diagrams. UV−Vis data were refined to obtain the simulated spectra for various Cu(II) complex forms using SPECFIT/32 software that adjusts the absorptivity and the stability constants of the species formed at equilibrium. SPECFIT uses factor analysis to reduce the absorbance matrix and to extract the eigenvalues prior to the multiwavelength fit of the reduced data set according to the Marquardt algorithm [28,49].

3.4. NMR measurements

NMR experiments were performed using a Bruker Ascend™ 400 MHz spectrometer equipped with a 5 mm automated tuning and a matching broad band probe (BBFO) with z-gradients. Samples used for NMR experiments were in the range 0.4 – 2.0 mM and dissolved in (90/10 (v/v) H_2O–D_2O. All NMR experiments were performed at 298 K in 5 mm NMR tubes. 2-D ^1H–^{13}C heteronuclear correlation spectra (HSQC) were acquired using a phase-sensitive sequence employing Echo-Antiecho-TPPI gradient selection with a heteronuclear coupling constant J_{XH} = 145 Hz, and shaped pulses for all 180° pulses on the f2 channel with decoupling during acquisition; sensitivity improvement and gradients in back-inept were also used. Relaxation delays of 2 s and 90° pulses of about 10 μs were applied for all experiments. Solvent suppression for ^1H and ^1H–^1H TOCSY experiments was achieved using excitation sculpting with gradients. The spin-lock mixing time of the TOCSY experiment was obtained with MLEV17. ^1H–^1H TOCSYs were performed using mixing times of 60 ms. ^1H–^1H ROESY spectra were acquired with spin-lock pulses duration in the range 200–250 ms. The assignments of the ^1H and ^{13}C were made by a combination of mono- and bi-dimensional and multinuclear NMR techniques ^1H–^1H TOCSY, ^1H–^{13}C HSQC and ^1H–^1H ROESY at different pH values. All NMR data were processed using the TopSpin (Bruker Instruments) software and analyzed using Sparky 3.11 and MestReNova 6.0.2 (Mestrelab Research S.L.) programs.

3.5. Molecular dynamics measurements

Extended peptide conformers were generated in Avogadro. Energy minimization was achieved using a restricted Hartree-Fock SCF, calculation was performed using Pulay DIIS + Geometric Direct Minimization, basis set: 3-21G(*), using Gaussian 16.

Subsequent calculations were carried out using available NAMD and VMD software. Structures were parameterized in CHARMM-GUI using the CHARMM36m force field. A rectangular waterbox was used to simulate the solvent behavior, sized as the protein size, and completed with KCl ions 0.05M to balance the charge of deprotonated amino acids. Ions were placed using the Monte-Carlo method. The simulations were carried out at a temperature of 298 K. Each simulation was executed for 1 μs (following an initial minimization) with structures calculated every 10 ps and written to a trajectory file. For the 1 μs simulation, 500000 time steps were recorded (2 fs = step size). Following the calculations, RMSD data plots relative to the extended, minimized initial structure were generated from the trajectory.

Model calculations for the Ni(II)-P29-38 complex were performed on the basis of the experimental evidences and the identification of specific ROE cross-correlations extracted from 2D ^1H-^1H ROESY spectra for the metal-bound system. At the pH value investigated no signals were

 doi:10.20944/preprints202305.0226.v1

detected in the aromatic region for the labile amide protons H_N, except for the Phe32 and His34 ring protons. ROE cross-peaks for the Ni(II)-P29-38 system, at 0.8 : 1 molar ratio, were assigned and the intensities converted into the maximal distances. Upper bounds u on the distance between two correlated hydrogen atoms were derived from the corresponding ROESY cross peak volumes V according to calibration curves $V=k/u^6$, with a constant k determined by using the cross-peak intensity of a selected H-H cross-peak between nuclei with known distance [39]. The structures shown in the RMSD trajectories were visualized and extracted using VMD and Chimera [50].

4. Conclusion

Zinc is an important cofactor for stabilizing protein structures and altering the substrate affinity of various metalloproteins. Zn^{2+} homeostasis could affect ACE-2 expression and binding to its active site is essential for its enzymatic activity [17]. It is very probable that the Zn^{2+} binding to ACE2 could influence the molecular structure of the receptor and therefore its binding affinity with SARS-CoV-2. At the same time, a large number of zinc-deficient patients are more prone to developing severe COVID19 [51,52]. The work presented here provides valuable insights into the complex coordination chemistry of Zn(II) and Cu(II) with three peptide fragments from the C-terminus of ACE-2 receptor, a region that play a crucial role in the binding with S protein of SARS-CoV-2. The study utilized a combination of potentiometry, UV-Vis and CD spectroscopy, and NMR techniques to investigate the formation and coordination mode of Zn(II) and Cu(II) ions with selected peptide fragments that mimic the interface recognition region of ACE2 for S. A Ni(II) diamagnetic analog was also studied as a Cu(II) probe since at high pH values the Cu(II)-systems experienced a severe line broadening in the NMR spectra, which prevented the detailed characterization of the species in the [N_{Im}, $3N^-_{amide}$] coordination mode. The results confirmed the bioinformatic previsions obtained by MIB2, which evidenced a highly specific region in ACE2 for zinc binding in the D30-Glu37 region. All experimental data indicate that this sequence is able to bind both metal ions in a very selective way. Moreover, the two long peptides mimicking the whole domain show the same coordination pattern as the shorter one, indicating the latter is an excellent model to study the coordinating abilities at the ACE2/S interface. Both metal ions can change the peptide conformation, which rearrange itself upon coordination with zinc and copper. Such structural modifications might interfere with the recognition mechanism of ACE2 and S protein, also considering that some of the residues taking part to or being perturbed by metal coordination play a crucial role in the hydrogen bond formation between the two proteins. These structural changes may decrease the affinity between ACE2 and S protein, and positively interfere in the mechanism through which the virus enters the cells. Therapies targeting ACE2 provide a general strategy to prevent and treat infections by SARS-CoV-2 and its variants, as well as other potential coronaviruses that use the ACE2 receptor as an entry route for viral invasion [53]. Whether it is possible to exploit this information in order to arrange a therapeutic strategy could be the topic of a new research and opens new perspectives in the treatment of COVID-19 in those patients who still experience severe symptoms after infection, or in case new aggressive variants would emerge.

Supplementary Materials: The following supporting information can be downloaded at the website of this paper posted on Preprints.org., Figure S1-S12; Table S1.

Author Contributions: Conceptualization, M.A.Z. and M.P.; methodology, M.P., A.P., B.O. and E.G.K; formal analysis, M.P., A.P., B.O.; investigation, M.P., A.P., B.O.; resources, M.A.Z, M.P., and E.G.K; writing—original draft preparation, M.P.; writing—review and editing, M.P., A.P., B.O., S.M., E.G.K., and M.A.Z.; visualization, M.P., A.P., B.O.; supervision, M.P.; funding acquisition, M.A.Z, S.M., A.P., and M.P. All authors have read and agreed to the published version of the manuscript.

Funding: S.M. and M.A.Z. acknowledge Università degli Studi di Sassari (UNISS) for the financial support received within the program "Fondo di Ateneo per la ricerca 2019, FAR 2019" (Rep. 2467, Prot. 94737 07/08/2019), and M.P. within the program "Fondo di Ateneo per la ricerca 2020, FAR

2020" (Rep. 2465, Prot. 0097985 01/09/2020). A.L. acknowledge Progetto UA2002DOTTRIC2021 articolo 9, comma 3, D.M. 8 febbraio 2013, n. 45, for financial support.

Data Availability Statement: All data generated or analyzed during this study are available under request.

Conflicts of Interest: The authors declare no conflict of interest.

References

1. Ni, W.; Yang, X.; Yang, D.; Bao, J.; Li, R.; Xiao, Y.; Hou, C.; Wang, H.; Liu, J.; Yang, D.; et al. Role of angiotensin-converting enzyme 2 (ACE2) in COVID-19. *Crit Care* **2020**, *24*, 422, doi:10.1186/s13054-020-03120-0.
2. Beyerstedt, S.; Casaro, E.B.; Rangel, E.B. COVID-19: angiotensin-converting enzyme 2 (ACE2) expression and tissue susceptibility to SARS-CoV-2 infection. *Eur J Clin Microbiol Infect Dis* **2021**, *40*, 905-919, doi:10.1007/s10096-020-04138-6.
3. Hamming, I.; Cooper, M.E.; Haagmans, B.L.; Hooper, N.M.; Korstanje, R.; Osterhaus, A.D.; Timens, W.; Turner, A.J.; Navis, G.; van Goor, H. The emerging role of ACE2 in physiology and disease. *J Pathol* **2007**, *212*, 1-11, doi:10.1002/path.2162.
4. Jackson, C.B.; Farzan, M.; Chen, B.; Choe, H. Mechanisms of SARS-CoV-2 entry into cells. *Nat Rev Mol Cell Biol* **2022**, *23*, 3-20, doi:10.1038/s41580-021-00418-x.
5. Perrotta, F.; Matera, M.G.; Cazzola, M.; Bianco, A. Severe respiratory SARS-CoV2 infection: Does ACE2 receptor matter? *Respir Med* **2020**, *168*, 105996, doi:10.1016/j.rmed.2020.105996.
6. Verdecchia, P.; Cavallini, C.; Spanevello, A.; Angeli, F. The pivotal link between ACE2 deficiency and SARS-CoV-2 infection. *Eur J Intern Med* **2020**, *76*, 14-20, doi:10.1016/j.ejim.2020.04.037.
7. Astuti, I.; Ysrafil. Severe Acute Respiratory Syndrome Coronavirus 2 (SARS-CoV-2): An overview of viral structure and host response. *Diabetes Metab Syndr* **2020**, *14*, 407-412, doi:10.1016/j.dsx.2020.04.020.
8. Hoffmann, M.; Kleine-Weber, H.; Pohlmann, S. A Multibasic Cleavage Site in the Spike Protein of SARS-CoV-2 Is Essential for Infection of Human Lung Cells. *Mol Cell* **2020**, *78*, 779-784 e775, doi:10.1016/j.molcel.2020.04.022.
9. Ozono, S.; Zhang, Y.; Ode, H.; Sano, K.; Tan, T.S.; Imai, K.; Miyoshi, K.; Kishigami, S.; Ueno, T.; Iwatani, Y.; et al. SARS-CoV-2 D614G spike mutation increases entry efficiency with enhanced ACE2-binding affinity. *Nat Commun* **2021**, *12*, 848, doi:10.1038/s41467-021-21118-2.
10. Yan, R.; Zhang, Y.; Li, Y.; Xia, L.; Guo, Y.; Zhou, Q. Structural basis for the recognition of SARS-CoV-2 by full-length human ACE2. *Science* **2020**, *367*, 1444-1448, doi:10.1126/science.abb2762.
11. Gong, W.; Parkkila, S.; Wu, X.; Aspatwar, A. SARS-CoV-2 variants and COVID-19 vaccines: Current challenges and future strategies. *Int Rev Immunol* **2022**, 1-22, doi:10.1080/08830185.2022.2079642.
12. Lan, J.; Ge, J.; Yu, J.; Shan, S.; Zhou, H.; Fan, S.; Zhang, Q.; Shi, X.; Wang, Q.; Zhang, L.; et al. Structure of the SARS-CoV-2 spike receptor-binding domain bound to the ACE2 receptor. *Nature* **2020**, *581*, 215-220, doi:10.1038/s41586-020-2180-5.
13. Shang, J.; Ye, G.; Shi, K.; Wan, Y.; Luo, C.; Aihara, H.; Geng, Q.; Auerbach, A.; Li, F. Structural basis of receptor recognition by SARS-CoV-2. *Nature* **2020**, *581*, 221-224, doi:10.1038/s41586-020-2179-y.
14. Lim, H.; Baek, A.; Kim, J.; Kim, M.S.; Liu, J.; Nam, K.Y.; Yoon, J.; No, K.T. Hot spot profiles of SARS-CoV-2 and human ACE2 receptor protein protein interaction obtained by density functional tight binding fragment molecular orbital method. *Sci Rep* **2020**, *10*, 16862, doi:10.1038/s41598-020-73820-8.
15. Li, W.; Zhang, C.; Sui, J.; Kuhn, J.H.; Moore, M.J.; Luo, S.; Wong, S.K.; Huang, I.C.; Xu, K.; Vasilieva, N.; et al. Receptor and viral determinants of SARS-coronavirus adaptation to human ACE2. *EMBO J* **2005**, *24*, 1634-1643, doi:10.1038/sj.emboj.7600640.
16. Ali, A.; Vijayan, R. Dynamics of the ACE2-SARS-CoV-2/SARS-CoV spike protein interface reveal unique mechanisms. *Sci Rep* **2020**, *10*, 14214, doi:10.1038/s41598-020-71188-3.
17. Wessels, I.; Rolles, B.; Rink, L. The Potential Impact of Zinc Supplementation on COVID-19 Pathogenesis. *Front Immunol* **2020**, *11*, 1712, doi:10.3389/fimmu.2020.01712.
18. Towler, P.; Staker, B.; Prasad, S.G.; Menon, S.; Tang, J.; Parsons, T.; Ryan, D.; Fisher, M.; Williams, D.; Dales, N.A.; et al. ACE2 X-ray structures reveal a large hinge-bending motion important for inhibitor binding and catalysis. *J Biol Chem* **2004**, *279*, 17996-18007, doi:10.1074/jbc.M311191200.
19. Fatouros, P.R.; Roy, U.; Sur, S. Implications of SARS-CoV-2 spike protein interactions with Zn-bound form of ACE2: a computational structural study. *Biometals* **2023**, 1-10, doi:10.1007/s10534-023-00491-z.
20. Lu, C.H.; Chen, C.C.; Yu, C.S.; Liu, Y.Y.; Liu, J.J.; Wei, S.T.; Lin, Y.F. MIB2: metal ion-binding site prediction and modeling server. *Bioinformatics* **2022**, *38*, 4428-4429, doi:10.1093/bioinformatics/btac534.
21. Benton, D.J.; Wrobel, A.G.; Xu, P.; Roustan, C.; Martin, S.R.; Rosenthal, P.B.; Skehel, J.J.; Gamblin, S.J. Receptor binding and priming of the spike protein of SARS-CoV-2 for membrane fusion. *Nature* **2020**, *588*, 327-330, doi:10.1038/s41586-020-2772-0.

22. Wu, K.; Peng, G.; Wilken, M.; Geraghty, R.J.; Li, F. Mechanisms of host receptor adaptation by severe acute respiratory syndrome coronavirus. *J Biol Chem* **2012**, *287*, 8904-8911, doi:10.1074/jbc.M111.325803.
23. Liu, N.; Zheng, L.; Xu, J.; Wang, J.; Hu, C.; Lan, J.; Zhang, X.; Zhang, J.; Xu, K.; Cheng, H.; et al. Reduced graphene oxide membrane as supporting film for high-resolution cryo-EM. *Biophysics Reports* **2021**, *7*, 227-238, doi:10.52601/bpr.2021.210007.
24. Han, P.; Su, C.; Zhang, Y.; Bai, C.; Zheng, A.; Qiao, C.; Wang, Q.; Niu, S.; Chen, Q.; Zhang, Y.; et al. Molecular insights into receptor binding of recent emerging SARS-CoV-2 variants. *Nat Commun* **2021**, *12*, 6103, doi:10.1038/s41467-021-26401-w.
25. Zheng, A.; Wu, L.; Ma, R.; Han, P.; Huang, B.; Qiao, C.; Wang, Q.; Tan, W.; Gao, G.F.; Han, P. A binding-enhanced but enzymatic activity-eliminated human ACE2 efficiently neutralizes SARS-CoV-2 variants. *Signal Transduct Target Ther* **2022**, *7*, 10, doi:10.1038/s41392-021-00821-y.
26. Peana, M.; Gumienna-Kontecka, E.; Piras, F.; Ostrowska, M.; Piasta, K.; Krzywoszynska, K.; Medici, S.; Zoroddu, M.A. Exploring the Specificity of Rationally Designed Peptides Reconstituted from the Cell-Free Extract of Deinococcus radiodurans toward Mn(II) and Cu(II). *Inorg Chem* **2020**, *59*, 4661-4684, doi:10.1021/acs.inorgchem.9b03737.
27. Magri, A.; Tabbi, G.; Di Natale, G.; La Mendola, D.; Pietropaolo, A.; Zoroddu, M.A.; Peana, M.; Rizzarelli, E. Zinc Interactions with a Soluble Mutated Rat Amylin to Mimic Whole Human Amylin: An Experimental and Simulation Approach to Understand Stoichiometry, Speciation and Coordination of the Metal Complexes. *Chemistry* **2020**, *26*, 13072-13084, doi:10.1002/chem.202002114.
28. Gampp, H.; Maeder, M.; Meyer, C.J.; Zuberbuhler, A.D. Calculation of equilibrium constants from multiwavelength spectroscopic data--II: SPECFIT: two user-friendly programs in basic and standard FORTRAN 77. *Talanta* **1985**, *32*, 257-264, doi:10.1016/0039-9140(85)80077-1.
29. Prenesti, E.; Daniele, P.G.; Prencipe, M.; Ostacoli, G. Spectrum–structure correlation for visible absorption spectra of copper(II) complexes in aqueous solution. *Polyhedron* **1999**, *18*, 3233-3241, doi:10.1016/S0277-5387(99)00279-X.
30. Lesiow, M.K.; Pietrzyk, P.; Bienko, A.; Kowalik-Jankowska, T. Stability of Cu(ii) complexes with FomA protein fragments containing two His residues in the peptide chain. *Metallomics* **2019**, *11*, 1518-1531, doi:10.1039/c9mt00131j.
31. Magri, A.; Munzone, A.; Peana, M.; Medici, S.; Zoroddu, M.A.; Hansson, O.; Satriano, C.; Rizzarelli, E.; La Mendola, D. Coordination Environment of Cu(II) Ions Bound to N-Terminal Peptide Fragments of Angiogenin Protein. *Int J Mol Sci* **2016**, *17*, doi:10.3390/ijms17081240.
32. Zoroddu, M.A.; Kowalik-Jankowska, T.; Medici, S.; Peana, M.; Kozlowski, H. Copper(II) binding to Cap43 protein fragments. *Dalton Trans* **2008**, 6127-6134, doi:10.1039/b808600a.
33. Zoroddu, M.A.; Kowalik-Jankowska, T.; Kozlowski, H.; Molinari, H.; Salnikow, K.; Broday, L.; Costa, M. Interaction of Ni(II) and Cu(II) with a metal binding sequence of histone H4: AKRHRK, a model of the H4 tail. *Biochim Biophys Acta* **2000**, *1475*, 163-168, doi:10.1016/s0304-4165(00)00066-0.
34. Kowalik-Jankowska, T.; Kadej, A.; Kuczer, M.; Czarniewska, E. Copper(II) complexes of the Neb-colloostatin analogues containing histidine residue structure stability biological activity. *Polyhedron* **2017**, *134*, 365-375, doi:10.1016/j.poly.2017.06.023.
35. Rowinska-Zyrek, M.; Wiech, A.; Wa Tly, J.; Wieczorek, R.; Witkowska, D.; Ozyhar, A.; Orlowski, M. Copper(II)-Binding Induces a Unique Polyproline Type II Helical Structure within the Ion-Binding Segment in the Intrinsically Disordered F-Domain of Ecdysteroid Receptor from Aedes aegypti. *Inorg Chem* **2019**, *58*, 11782-11792, doi:10.1021/acs.inorgchem.9b01826.
36. Medici, S.; Peana, M.; Nurchi, V.M.; Zoroddu, M.A. The involvement of amino acid side chains in shielding the nickel coordination site: an NMR study. *Molecules* **2013**, *18*, 12396-12414, doi:10.3390/molecules181012396.
37. Peana, M.; Zdyb, K.; Medici, S.; Pelucelli, A.; Simula, G.; Gumienna-Kontecka, E.; Zoroddu, M.A. Ni(II) interaction with a peptide model of the human TLR4 ectodomain. *J Trace Elem Med Biol* **2017**, *44*, 151-160, doi:10.1016/j.jtemb.2017.07.006.
38. Jones, C.E.; Klewpatinond, M.; Abdelraheim, S.R.; Brown, D.R.; Viles, J.H. Probing copper2+ binding to the prion protein using diamagnetic nickel2+ and 1H NMR: the unstructured N terminus facilitates the coordination of six copper2+ ions at physiological concentrations. *J Mol Biol* **2005**, *346*, 1393-1407, doi:10.1016/j.jmb.2004.12.043.
39. Peana, M.F.; Medici, S.; Ledda, A.; Nurchi, V.M.; Zoroddu, M.A. Interaction of Cu(II) and Ni(II) with Ypk9 protein fragment via NMR studies. *ScientificWorldJournal* **2014**, *2014*, 656201, doi:10.1155/2014/656201.
40. Irving, H.; Williams, R.J.P. 637. The stability of transition-metal complexes. *Journal of the Chemical Society (Resumed)* **1953**, 3192-3210, doi:10.1039/JR9530003192.
41. Rae, T.D.; Schmidt, P.J.; Pufahl, R.A.; Culotta, V.C.; O'Halloran, T.V. Undetectable intracellular free copper: the requirement of a copper chaperone for superoxide dismutase. *Science* **1999**, *284*, 805-808, doi:10.1126/science.284.5415.805.

42. Maret, W. Analyzing free zinc(II) ion concentrations in cell biology with fluorescent chelating molecules. *Metallomics* **2015**, *7*, 202-211, doi:10.1039/c4mt00230j.
43. Gran, G.; Dahlenborg, H.; Laurell, S.; Rottenberg, M. Determination of the equivalent point in potentiometric titrations. *Acta chem. scand* **1950**, *4*, 559-577, doi:10.3891/acta.chem.scand.04-0559.
44. Gans, P.; Sabatini, A.; Vacca, A. Investigation of equilibria in solution. Determination of equilibrium constants with the HYPERQUAD suite of programs. *Talanta* **1996**, *43*, 1739-1753, doi:10.1016/0039-9140(96)01958-3.
45. Gans, P.; Sabatini, A.; Vacca, A. Superquad - a new computer program for determination of stability constants of complexes by potentiometric titration. *Inorganica Chimica Acta* **1983**, *79*, 219-220, doi:10.1016/S0020-1693(00)95255-1.
46. Brown, P.L.; Ekberg, C. *Hydrolysis of metal ions*; John Wiley & Sons: 2016.
47. Mesmer, C.F.B.a.R.S. The Hydrolysis of Cations. John Wiley & Sons, New York, London, Sydney, Toronto 1976. 489 Seiten. *Berichte der Bunsengesellschaft für physikalische Chemie* **1977**, *81*, 245-246, doi:10.1002/bbpc.19770810252.
48. Alderighi, L.; Gans, P.; Ienco, A.; Peters, D.; Sabatini, A.; Vacca, A. Hyperquad simulation and speciation (HySS): a utility program for the investigation of equilibria involving soluble and partially soluble species. *Coordination Chemistry Reviews* **1999**, *184*, 311-318, doi:10.1016/S0010-8545(98)00260-4.
49. Rossotti, F.J.C.; Rossotti, H.S.; Whewell, R.J. The use of electronic computing techniques in the calculation of stability constants. *Journal of Inorganic and Nuclear Chemistry* **1971**, *33*, 2051-2065, doi:10.1016/0022-1902(71)80567-5.
50. Pettersen, E.F.; Goddard, T.D.; Huang, C.C.; Couch, G.S.; Greenblatt, D.M.; Meng, E.C.; Ferrin, T.E. UCSF Chimera--a visualization system for exploratory research and analysis. *J Comput Chem* **2004**, *25*, 1605-1612, doi:10.1002/jcc.20084.
51. Jothimani, D.; Kailasam, E.; Danielraj, S.; Nallathambi, B.; Ramachandran, H.; Sekar, P.; Manoharan, S.; Ramani, V.; Narasimhan, G.; Kaliamoorthy, I.; et al. COVID-19: Poor outcomes in patients with zinc deficiency. *Int J Infect Dis* **2020**, *100*, 343-349, doi:10.1016/j.ijid.2020.09.014.
52. Wessels, I.; Rolles, B.; Slusarenko, A.J.; Rink, L. Zinc deficiency as a possible risk factor for increased susceptibility and severe progression of Corona Virus Disease 19. *British Journal of Nutrition* **2022**, *127*, 214-232, doi:10.1017/S0007114521000738.
53. Oudit, G.Y.; Wang, K.; Viveiros, A.; Kellner, M.J.; Penninger, J.M. Angiotensin-converting enzyme 2-at the heart of the COVID-19 pandemic. *Cell* **2023**, *186*, 906-922, doi:10.1016/j.cell.2023.01.039.